

THESIS FOR THE DEGREE OF DOCTOR OF PHILOSOPHY

Mesospheric measurements using microwave spectroscopy

Ole Martin Christensen



Department of Earth and Space Sciences
CHALMERS UNIVERSITY OF TECHNOLOGY
Gothenburg, Sweden, 2015

Mesospheric measurements using microwave spectroscopy

Ole Martin Christensen

ISBN 978-91-7597-235-0

© Ole Martin Christensen, 2015.

Doktorsavhandlingar vid Chalmers tekniska högskola

Ny serie nr. 3916

ISSN 0346-718X

Department of Earth and Space Sciences

Chalmers University of Technology

SE - 412 96 Gothenburg, Sweden

Phone + 46 (0)31 772 1000

Printed by Chalmers Reproservice

Chalmers University of Technology

Gothenburg, Sweden 2015



The text of this work is licensed under a Creative Commons Attribution 3.0 Unported License. All pictures and figures are property of their respective owners.

Cover: Description of Cover

Mesospheric measurements using microwave spectroscopy

Ole Martin Christensen

Department of Earth and Space Sciences

Chalmers University of Technology

Abstract

The mesosphere is an altitude region of the atmosphere, covering altitudes between about 50 km to 100 km. Improved understanding of this area of the atmosphere offers possibilities of increasing the accuracy of weather forecast and climate models. Continuous measurements at these altitudes are difficult as neither balloon nor airplanes can reach such heights. However, by remotely measuring thermal emission emitted in the microwave region, properties such as the atmospheric temperature and the abundance of species such as water vapour and ozone, can be determined from instruments placed on the ground or on satellites.

In this thesis microwave spectroscopy is used to measure carbon monoxide above the Onsala Space Observatory located south of Gothenburg, Sweden. The results of the measurements are compared to, and found in good agreement with, co-located data from satellite instruments. A new inversion technique is also demonstrated which integrates the temporal averaging of spectra directly into the retrieval. This shows that ground-based microwave instruments are well suited for mesospheric monitoring, which will become more important in the future as many of the satellite instruments used in the comparison are slated for retirement, with no immediate replacements planned.

Microwave spectroscopy can also be used in studies related to polar mesospheric clouds. These are clouds that form in the uppermost part of the summer mesosphere and are extremely sensitive to temperature changes in the background atmosphere. In this thesis tomographic measurements from the sub-millimetre radiometer on-board the Odin satellite are used to retrieve 2-D images of the background temperature and water vapour around these clouds. Combining these results with measurements of ice content and ice particle sizes in the clouds from Odin's other instrument OSIRIS, allows us to investigate the relationship between the horizontal and vertical features in the clouds and their background atmosphere with a hitherto unsurpassed resolution.

Keywords: remote sensing, mesosphere, retrieval, microwave spectroscopy, temperature, carbon monoxide, ozone, water vapour, polar mesospheric clouds, noctilucent clouds

APPENDED PAPERS

The thesis is based on the following articles:

- P. Forkman, O.M. Christensen, P. Eriksson, J. Urban, B. Funke. Six years of mesospheric CO estimated from ground-based frequency-switched microwave radiometry at 57° N compared with satellite instruments. *Atmos. Meas. Tech.*, 5, 2827-2841, doi:10.5194/amt-5-2827-2012, 2012.
- O.M. Christensen, P. Eriksson. Time series inversion of spectra from ground-based spectrometers. *Atmos. Meas. Tech.*, 6, 1597-1609, doi:10.5194/amt-6-1597-2013, 2013.
- P. Forkman, O.M. Christensen, P. Eriksson, B. Billade, V. Vassilev, V. M. Shulga. A compact receiver system for simultaneous measurements of mesospheric CO and O₃. *Manuscript submitted to Geosci. Instrum. Method. Data Syst.*,
- O. M. Christensen , P. Eriksson , J. Urban, D. Murtagh , K. Hultgren , J. Gumbel. Tomographic retrieval of water vapour and temperature around polar mesospheric clouds using Odin-SMR. *Atmos. Meas. Tech.*, 8, 1981-1999, doi:10.5194/amt-8-1981-2015, 2015.
- O. M. Christensen, S. Benze , P. Eriksson, J. Gumbel, L. Megner, D. P. Murtagh. The relationship between Polar Mesospheric Clouds and their background atmosphere as observed by Odin-SMR and Odin-OSIRIS.. *Manuscript prepared for Atmos. Chem. Phys.*.

CONTENTS

CHAPTER 1 – INTRODUCTION	1
CHAPTER 2 – THE ATMOSPHERE	5
2.1 Structure of the atmosphere	5
2.2 Polar Mesospheric Clouds	10
2.3 Mesospheric Chemistry	12
2.4 The Changing Middle Atmosphere	16
CHAPTER 3 – MEASUREMENT PRINCIPLES	21
3.1 Blackbody radiation	21
3.2 Absorption and emission by gases	23
3.3 The radiative transfer equation	24
3.4 1-D retrievals	25
3.5 Limitations of an retrieval	30
3.6 Multidimensional retrievals	32
3.7 Instrumental error sources	36
CHAPTER 4 – INSTRUMENTS	39
4.1 Measuring the atmosphere	39
4.2 The microwave spectrometer	40
4.3 Ground-based instruments	43
4.4 Satellite instruments	50
CHAPTER 5 – SUMMARY OF PAPERS	61
5.1 Summary Paper A	61
5.2 Summary Paper B	62
5.3 Summary Paper C	62
5.4 Summary Paper D	63
5.5 Summary Paper E	63
REFERENCES	65
PAPER A	1
PAPER B	17
PAPER C	31
PAPER D	63

PREFACE

As a young graduate student getting into atmospheric physics, I once asked my then supervisor Dr. Patrick Espy: “So what about global warming, is it real?”. This question might sound naive and poorly formulated, but it symbolises one of the most important environmental questions of our time. And though a consensus exists in the scientific community (Cook et al., 2013), for the layperson it is not necessarily as clear. As a good professor, Dr. Espy did not give me a straight answer to the question, but rather gave me a book and said, “Read this”. The book was “Climate Process and Change” by Edward Bryant, an excellent summary of the myriad of papers discussing how different phenomena affect Earth’s climate. Of all the figures in that book, one struck me as especially intriguing. It was a figure showing the temperature changes the last 50 years at 50 hPa pressure (roughly an altitude of 20 km), and it showed a cooling trend! In the words of the author:

“The records show a tendency for cooling by -0.5 to -1°C over this timespan [...] As a first approximation the stratospheric temperature record supports enhanced ‘greenhouse’ warming better than does the surface record.”

This cooling was for me completely counter-intuitive, but seeing this I was finally convinced that the greenhouse effect is real, and that human emission of greenhouse gases have had a significant impact on the earth over the last 50 years.

As I have gained further knowledge about the fascinating middle atmosphere I have realised that the truth is indeed more complicated than the impression given by the paragraph from the aforementioned book. The middle atmospheric temperatures are affected by much more than just the greenhouse effect, and drawing clear conclusions about trends from the limited data we have, especially as we look at altitudes above 50 km, is not easy. But if understanding and presenting data from this region can help convince people (like myself) that human activities not only affect the environment down here at ground level, but have a significant impact on the entire atmosphere, the time and effort we as scientists put into this field is well worth it.

This thesis represents the effort put forth by myself and my co-authors over the last five years to advance the field of middle atmospheric physics. We have cross-compared instruments, developed new measurement techniques, and generated unique datasets of measurement results covering different mesospheric phenomena. I hope you, the reader, can find these results as fascinating as me, and that they can inspire further work and advancements within the field of middle atmospheric science.

Ole Martin Christensen

CHAPTER 1

Introduction

During February 2009, massive snowfalls across Europe and the United States paralysed the transportation infrastructure, resulting in large socio-economic cost on both sides of the Atlantic (Jones and Gillan, 2009). Rather dramatically, the blizzard was even dubbed “snowmageddon” by the U.S. President (Morgan and Beech, 2010). Meteorologists however knew very well that such a cold streak could happen, due to a phenomenon occurring much higher in the atmosphere, known as a sudden stratospheric warming. This phenomenon is characterised by a reversal of the westerly winds in the stratosphere, 30 km over the winter pole, with a following sudden increase of the stratospheric temperature (McInturff, 1978). This breakup of the so called polar vortex is usually followed by a reversal of tropospheric winds within a few days up to two months later (Baldwin and Dunkerton, 2001) leading to cold weather, especially in western Europe.

Understanding the atmospheric processes occurring in the region called the middle atmosphere, between 10 and 100 km above the Earth’s surface, can provide vital clues in to what’s happening in the lower atmosphere. When the Canadian Meteorological Centre extended the roof of their medium-range weather forecast model from 10 (~30 km) to 0.1 hPa (~65 km) a significant improvement was seen not only in their high altitude forecast, but the accuracy of the forecast was increased all the way down to 500 hPa (~5 km) (Charron et al., 2012). Other medium-range weather forecast models are also extending their upper limit. The European Centre for Medium-Range Weather Forecasts’ Integrated Forecast System ensemble model was, for example, recently (Nov. 2013) extended to cover altitudes up to 0.01 hPa (~80 km). The fact that these models are going higher and higher to improve their seasonal forecasts, despite the increased computational cost this entails, is a clear indication of the importance of understanding, measuring and quantifying the processes in this region of the atmosphere.

The middle atmosphere does not only give us information about the daily weather, but contains clear evidence of human influence on the Earth’s atmosphere. Scientists have linked the drastic drop in the stratospheric ozone concentrations since the 70s to



Figure 1.1: Polar Mesospheric Clouds over Stockholm (courtesy of Kristell Perot).

the release of chlorofluorocarbons (e.g. Stolarski and Cicerone (1974)). And in 1987 the Montreal Protocol was signed, committing countries to phase out the production of these ozone depleting substances. But, it is only now, almost 30 years later, that indications of a recovery can be seen (Jones et al., 2009). However, as the effect of reducing emissions of ozone depleting substances is beginning to show, the effects of the anthropogenically released greenhouse gases are making themselves ever clearer. There have for example been studies indicating that the aforementioned breakup of the polar vortex will occur more often in the future as the loss of Arctic sea ice modifies the underlying wave structures of the atmosphere, weakening the vortex (Kim et al., 2014).

This thesis is mainly concerned with the region of the atmosphere called the mesosphere which covers altitudes from roughly 50 to 100 km. Just as the rest of the atmosphere it is expected to change in the future. The mesosphere is, unlike the lower atmosphere, expected to cool with a predicted reduction in the mean temperature of 10 K with a doubling of CO₂ concentrations (Roble and Dickinson, 1989). Experimental data from a number of different measurement methods supports this value, with a general reduction in mesospheric temperature of a few degrees per decade (Beig et al., 2003) being measured. This cooling of the atmosphere means that its density will increase, effectively shrinking the size of the atmosphere. This has for example been seen in a reduced satellite drag over the last decades (Keating et al., 2000).

The cooling of the mesosphere will also affect many other features of the mesosphere. One of the most mundane and easily observed of these phenomena are polar mesospheric clouds. These clouds form in the upper part of the mesosphere (around 85 km) during the summer season in polar regions. With decreasing temperatures it is

expected that we will see more of these clouds in the future, some scientists dubbing them a “Miners Canary” of global change (Thomas, 1996). But establishing such a trend has turned out to be harder than anticipated, with the most recent studies showing only a small positive trend in overall ice abundance (Hervig and Stevens, 2014), and no significant trend after the 1990s (DeLand and Thomas, 2015).

The reasons that such trends are hard to establish are many. First of all, the region where they form has not shown the same clear cooling trend as the rest of the mesosphere (Beig et al., 2003). Furthermore cloud formation is affected by a myriad of other factors such as amount of available water vapour, available condensation nuclei (Hunten et al., 1980), solar activity (Thomas et al., 1991; von Savigny et al., 2007), diurnal variations (Fiedler et al., 2005) and space traffic (Stevens et al., 2003). The relative importance of each factor is still in open scientific debate (e.g. Megner (2011)), and despite the fact that scientist have been studying these clouds for over 130 year (Leslie, 1885; Backhouse, 1885; Jesse, 1885) much still remains unknowns about them.

Thus, whether its monitoring cloud formation, mesospheric weather or the ozone layer, measurements are needed to see new connections, monitor changes and validate models. This thesis is based on a set of 5 papers concerning measurements of the mesosphere (Part 2). The first three revolves around the ground-based microwave radiometers located at the Onsala Space Observatory south of Gothenburg Sweden. These are instruments which are operating continuously and have previously been used both to assess atmospheric models (Forkman et al., 2003a), as well as the aforementioned 2009/2010 sudden stratospheric warming (Scheiben et al., 2012). Paper A and C focus on validating the ground-based radiometers against satellite based instruments. And in Paper B a novel approach to generate time-series from such instruments is developed. Papers D and E concern a set of measurements of polar mesospheric clouds performed by the Odin satellite in 2010 and 2011. Paper D describes the method used to extract information about the background atmosphere from these measurements, whereas Paper E discusses how the background atmosphere influences the clouds. But before the papers are introduced, an introduction to the broader scientific context into which these papers have been published will be given (Part 1). Here the basic methods and theories underlying the papers are described in detail, and the scientific questions they pose will be put into a broader context.

CHAPTER 2

The Atmosphere

The atmosphere is the layer of air surrounding the Earth. It constitutes less than one millionth the mass of the Earth, but is essential for all land-based life. It provides fresh water through the hydrological cycle, its ozone layer protects us from dangerous UV radiation, and greenhouse gases trap heat in the atmosphere resulting in a mild and temperate climate. Understanding how the atmosphere works helps us answer interesting scientific questions ranging from why the dinosaurs became extinct, to what the weather will be tomorrow, or to predict the climate a 100 years from now.

The middle atmosphere, which is the atmospheric layer between roughly 10 and 100 km, is interesting as it offers many unique atmospheric phenomena to study. The depletion of the ozone layer has illustrated that humans can have large scale impact on the atmosphere. Understanding the dynamics of the middle atmosphere can give an indication of how accurately climate models represent small scale features such as atmospheric waves, and due to the strong influence of solar radiation has on the middle atmosphere it can provide insights into how solar variations affect the climate. This chapter will provide a short introduction to the processes important to the middle atmosphere, and highlight some of the important scientific questions relevant to the middle atmosphere with a particular focus on the mesosphere.

2.1 Structure of the atmosphere

The atmosphere extends from sea-level and all the way to space¹. It is kept in place around Earth by the gravitational force. At large, the atmosphere is in the state of hydrostatic equilibrium. This means that the gravitational force is balanced by the vertical pressure gradient, or buoyancy force. As a result the pressure decreases exponentially with altitude, as does the density due to the compressibility of air.

It is customary to divide the atmosphere into layers based on the vertical tem-

¹A precise definition of outer space does not exist, but to be awarded the astronaut badge by NASA one has to have been at altitudes above 100 km (Darrin and O'Leary, 2009)

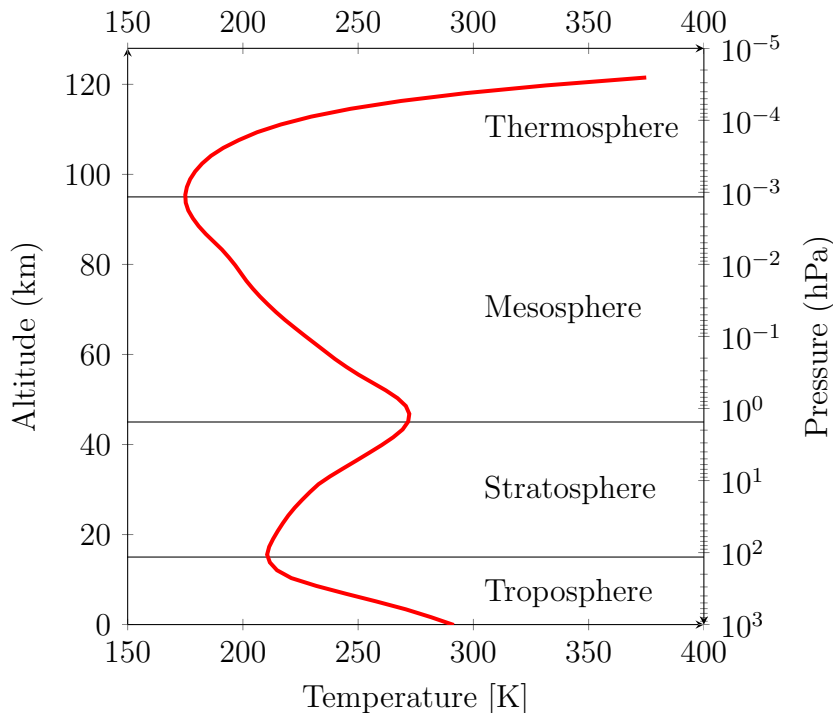


Figure 2.1: Temperature and layers of the atmosphere. The temperature data is taken from the COSPAR International Reference Atmosphere (CIRA-86), at 40° N, June (Rees et al., 1990).

perature gradient. This is shown in figure 2.1. The lowermost layer is called the troposphere and is characterised by a decrease in temperature with altitude. Within this layer we find most of the everyday atmospheric phenomena such as clouds and precipitation. At around 10-15 km the increased photolysis of ozone causes the temperature to increase with height. The resulting layer is called the stratosphere. This part of the atmosphere is home to the ozone layer which protects the ground from DNA damaging UV radiation. Above 50 km, in the layer known as the mesosphere, the temperature is decreasing with altitude again. This layer is home to the coldest area of the atmosphere, the summer mesopause. The middle atmosphere is a collective term for both the stratosphere and mesosphere. Above the mesopause, in the thermosphere, the temperature increases with height. Separating these layers are the tropopause (~ 15 km), stratopause (~ 50 km) and mesopause (~ 95 km), respectively, shown by the horizontal lines in figure 2.1.

Across the middle atmosphere atoms and molecules are ionised by short wavelength solar radiation or precipitating energetic particles. This means that the mesosphere and thermosphere can be considered a weakly ionised plasma collectively known as the ionosphere. The ionosphere stretches from approximately 60 km up to about 1000 km and is itself divided into layers based on the vertical profile of mean electron density (Brasseur and Solomon, 2005). These charged particles can

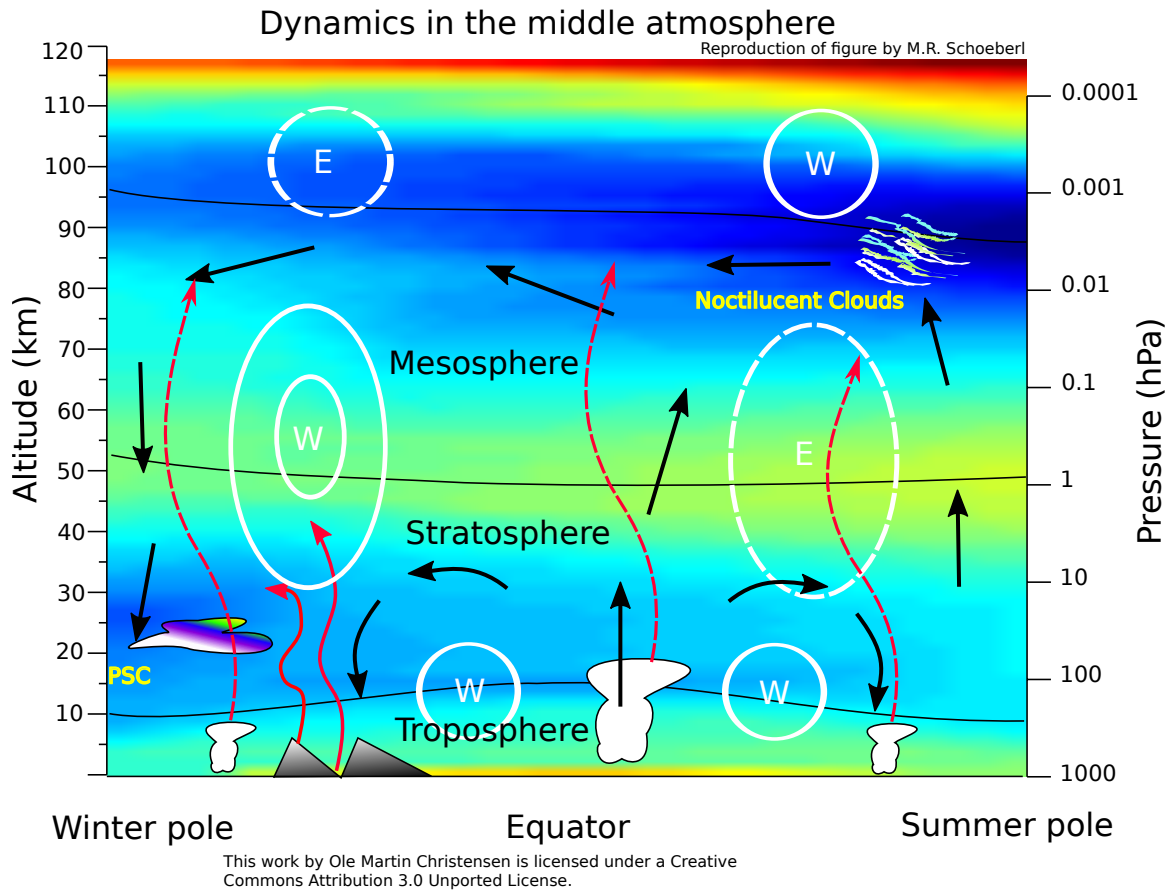


Figure 2.2: An illustration of the general circulation of the middle atmosphere. Background contours show the zonal mean temperature from CIRA-86 during the solstice, white lines depicts the zonal mean wind as easterlies and westerlies and the dashed and solid red lines indicate gravity and planetary waves respectively, finally the black arrows illustrate the mean residual circulation.

affect the chemistry of the middle atmosphere, and reactions involving ions are for example known to create NO which in turn modifies the ozone concentrations (see section 2.3.2). Furthermore atmospheric ions have been suggested as possible cloud condensation nuclei for polar mesospheric clouds (Witt, 1969), and it has even been suggested that ions may modify the nucleation processes of tropospheric clouds (Svensmark and Friis-Christensen, 1997).

2.1.1 General Circulation

The principal driver of air movement on the Earth is the sun. As the incoming solar energy varies with latitude, an energy imbalance is created which is restored by transport of energy from the equator to the poles. Due to the rotation of the Earth, topographic features, and the chemical composition of the atmosphere, the

general circulation follows a set of intricate patterns rather than a direct poleward flow. Figure 2.2 shows the zonal mean temperature distribution of the atmosphere together with the major middle-atmospheric general circulation patterns.

The two most important features of the general circulation are the Brewer-Dobson circulation in the stratosphere and the meridional pole to pole circulation in the mesosphere. The Brewer-Dobson circulation is driven by the deposition of momentum by planetary waves breaking in the stratosphere. Planetary-, or Rossby waves, are large scale waves with wavelengths on the order of the planetary circumference. These planetary wave modes can be forced by for example large topographic features such as the Rocky mountains or the Himalayas. When these waves break, they deposit westward momentum in the stratosphere, which through the Coriolis force leads to a poleward transport in the upper stratosphere, creating the Brewer-Dobson circulation (Holton, 1992).

In the mesosphere the circulation is driven by the breaking of gravity waves. Gravity waves are smaller scale waves generated by topographic features or convective activity in the troposphere. Though waves carrying both eastward and westward momentum can propagate upwards, gravity waves are filtered in the stratosphere by the mean zonal winds. This filtering occurs since gravity waves with a phase velocity equal to the velocity of the background winds cannot propagate (Lindzen, 1981). From figure 2.2 we see that the prevailing stratospheric winds are westerly in the winter and easterly in the summer. This means that gravity waves with westward phase speeds are filtered out in the summer and those with eastward speeds are filtered out in the winter. Thus when the waves finally break in the in the mesosphere, a net westward momentum will be deposited in the winter hemisphere and net eastwards in the summer hemisphere. The result of this breaking is a single cell transporting air from the summer to the winter pole. This residual transport modifies the temperature distribution, adiabatically cooling the atmosphere in areas of ascending air, and heating it in areas of descending air. This effect is seen particularly in the summer mesopause (~ 90 km) where the adiabatic cooling of ascending air makes it extremely cold despite 24 h solar heating (Brasseur and Solomon, 2005).

The meridional, pole to pole circulation in the mesosphere means that the middle atmosphere of the two hemispheres are intimately interconnected. In particular a connection has been shown between the winter stratosphere, and summer mesopause region. In winters with high planetary wave activity, the westerly winds in the stratosphere experience an increased amount of drag, which in the end results in weaker winds and a stronger residual circulation. The weaker winds decrease the effectiveness of gravity wave filtering, resulting in a net weaker mesospheric pole to pole circulation, which in turn means that the summer mesopause becomes warmer. Evidence of this has for example been found by comparing observations of polar mesospheric clouds in the summer hemisphere to the variability of the polar vortex in winter hemisphere (Karlsson et al., 2007). This inter-hemispheric coupling thus illustrates how examining the middle atmosphere can improve our understanding of the atmosphere as a whole.

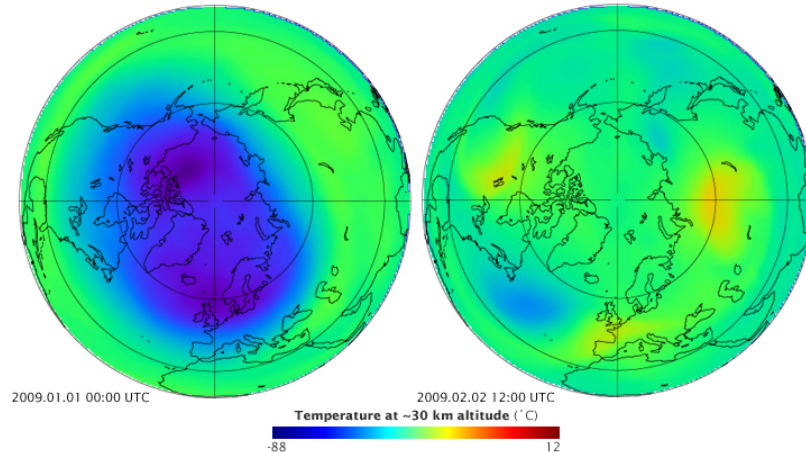


Figure 2.3: Temperature at ~ 30 km before (left) and after (right) the sudden stratospheric warming of January 2009 from assimilated weather observations (NASA’s Earth Observatory, 2009).

2.1.2 Polar Vortex

A particular feature arising from the general middle atmospheric circulation is the large scale westerly winds in the winter hemisphere stretching from the low stratosphere all the way up into the mesosphere. This westerly jet manifests itself as a vortex around the winter pole, and is as such appropriately named the Polar Vortex. These strong westerly winds result in a strong isolation of the polar air masses. Since the solar heating is limited during the winter months, the isolated air inside the vortex cools down, creating a strong temperature gradient between the polar air and the surrounding regions. This is seen clearly in the left panel of figure 2.3 where typical mid-winter temperatures at 30 km are shown. Another way to illustrate this isolation is by calculating the potential vorticity of air parcels around the winter pole. Assuming no diabatic heating or frictional forces, a parcel of air will follow the isocontour of potential vorticity. Hence, potential vorticity contours inside the vortex tend to stay inside the vortex (see figure 2.5b).

However, during some winters, the stable eastward flow of the vortex can be disturbed by planetary- and gravity wave activity, resulting in a partial or complete breakdown of the polar vortex. This phenomenon is known as a sudden stratospheric warming and can be divided into major and minor events. A major event is defined as an event where there is a sudden temperature increase at latitudes poleward of 60 degree and altitudes higher than the 10 hPa level followed by a reversal of the stratospheric winds. If a temperature increase happens without the complete reversal of the winds the event is classified as a minor warming.

Both major and minor warnings have significant impact on the middle atmosphere. For example, the downward motion of air occurring after these events can transport reactive species, such as NO, down from the mesopause. This can in turn result in an increased O₃ destruction in the upper stratosphere (e.g. Pérot et al. (2014)).

It has even been shown that sudden stratospheric warmings have significant effect on tropospheric weather patterns (Baldwin and Dunkerton, 2001). Hence, sudden stratospheric warming is thus an example of how intertwined the different layers of the atmosphere can be.

2.2 Polar Mesospheric Clouds

As explained, the upper mesopause becomes extremely cold in summer due to the large scale meridional circulation, reaching temperatures below 130 K. This means that clouds can form despite the relatively low water vapour concentrations in the mesosphere. Due to the low pressure, liquid water cannot exist, and the resulting clouds are made of ice and are called Polar Mesospheric-, or Noctilucent, Clouds (PMC). These clouds coincide with a phenomenon known as Polar Mesospheric Summer Echoes (PMSE), where small ice particles interact with the ionospheric plasma resulting in charge inhomogeneities that can be detected by radars (Rapp and Lübken, 2004). An overview of the properties and processes of these mesospheric ice particles is shown in figure 2.4.

2.2.1 Saturation

For PMCs to form, the amount of water vapour in the atmosphere must exceed that which the atmosphere can hold. This amount is usually given by the saturation vapour pressure over ice, p_{ice} , and the ratio of the partial pressure of water vapour to the saturation vapour pressure is known as the saturation ratio, S . Assuming that the volume of ice is much smaller than the volume of water vapour the saturation pressure can be calculated through the Clausius-Clapeyron relation (Murphy and Koop, 2005)

$$\frac{d \ln(p_{ice})}{dT} = \frac{L_{ice}(T)}{RT^2}, \quad (2.1)$$

where $L_{ice}(T)$ is the latent heat of sublimation of ice and R the molar gas constant. The temperature dependence of the latent heat means that integrating equation 2.1 becomes non-trivial, and thus several empirical expressions based on direct measurements of p_{ice} or numerical integration of the Clausius-Clapeyron relation have been used for mesospheric conditions. Furthermore, the latent heat of ice sublimation will depend on the crystalline structure of ice with the thermodynamic stable hexagonal ice having the lowest vapour pressure, while other forms such as amorphous and cubic crystalline have larger saturation pressures. The exact vapour pressure over ice for mesospheric conditions is still unknown, adding significant uncertainties to any quantitative description of PMC microphysics (Rapp and Thomas, 2006).

2.2.2 Nucleation

For a cloud to form it is not enough for the atmosphere to be just supersaturated, i.e. the partial pressure of water is above that of the saturation vapour pressure. Due

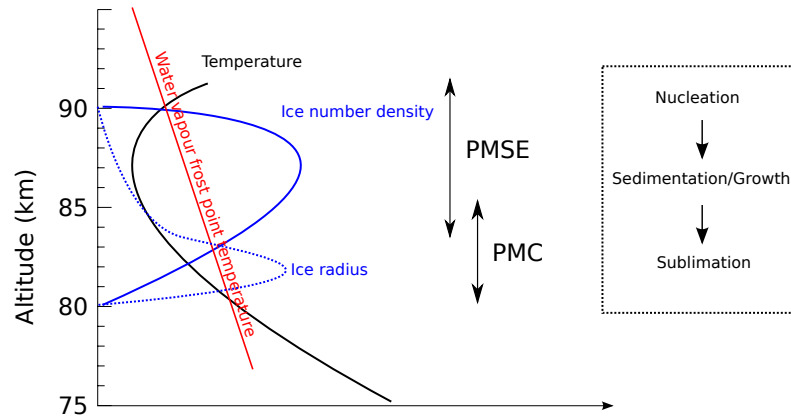


Figure 2.4: Schematic overview of the processes involved in the formation of Polar Mesospheric Clouds, adapted from Rapp and Thomas (2006).

to the surface tension of ice, extra energy is required for vapour to deposit onto a curved surface, rather than a flat one. This effect is known as the Kelvin effect, and to account for it the previously mentioned saturation vapour pressure needs to be adjusted through the Kelvin equation

$$p_{ice}(r) = p_{ice}(\infty) \cdot \exp^{2m\sigma/\rho kTr}, \quad (2.2)$$

where $p_{ice}(\infty)$ is the saturation vapour pressure above a flat surface, m the molecular weight of water, σ the surface free energy, ρ the density of the ice particle, k the Boltzmann constant and r the radius of the nucleation kernel. This equation implies that for water vapour to spontaneously deposit into ice, i.e. r is on the order of a single water molecule, the saturation ratio needs to be exceedingly high. This formation process is known as homogeneous nucleation, and for mesospheric conditions, very low temperatures (< 100 K) and high concentrations of water vapour (> 10 ppmv) are needed for this process to start (Rapp and Thomas, 2006).

The conditions needed for homogeneous nucleation do not occur in the mesopause, and thus a condensation nucleus on which the water molecule can deposit into ice is needed. The formation of clouds by deposition/condensation onto a nucleus is known as heterogeneous nucleation, and this process requires significantly lower saturation ratios to start since $r \gg 0$ in equation 2.2. Several different candidates have been suggested as seeds for polar mesospheric cloud formation. These include large proton hydrate clusters (Witt, 1969), sulphate aerosol particles (Mills et al., 2005), soot particles (Pueschel et al., 2000), sodium salts (Plane, 2000) and meteoric dust (Hunten et al., 1980). The available number of nucleation particles is thus highly uncertain, and estimations vary by several orders of magnitude which can greatly affect the amount of ice content in the clouds predicted by cloud models (Rapp and Thomas, 2006).

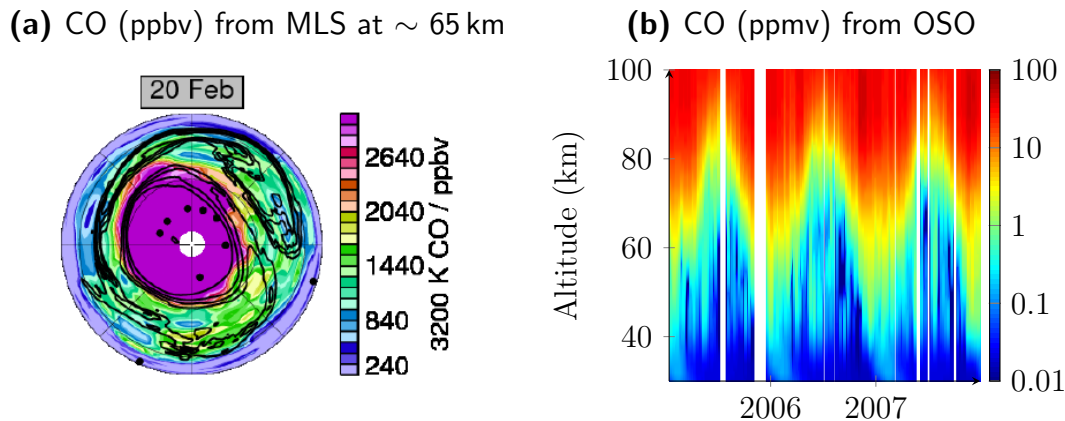


Figure 2.5: Volume mixing ratio of CO in the middle atmosphere. Right: The horizontal distribution the 20 January 2006 from 0-90 °N at roughly 65 km (potential temperature = 3200 K) measured by the microwave limb sounder on board Aura (Manney et al., 2009). The black lines are isocontours of potential vorticity. Left: The seasonal variation of CO above OSO measured with the 115 GHz radiometer.

2.3 Mesospheric Chemistry

2.3.1 The chemistry of mesospheric CO

One way to investigate the dynamics of the middle atmosphere is to trace the concentration of gases with long photochemical lifetimes, i.e. that the gas is not rapidly destroyed (or created) by either chemical or photochemical processes. If such a gas is created locally, the distribution of this gas across the atmosphere will be determined mainly by the transport, and it can as such act as a tracer of air movements.

One such tracer gas is carbon monoxide, which has a photochemical lifetime in the mesosphere in the order of several months to a year (Brasseur and Solomon, 2005). In the stratosphere it is produced by oxidation of methane and in the thermosphere and mesopause region it is produced through the photolysis of carbon dioxide



The only important destruction mechanism of carbon monoxide in the mesosphere is the reaction with OH



Figure 2.5a shows the concentration of CO at around 65 km during the Arctic winter measured by Aura-MLS (Manney et al., 2009). The aforementioned polar vortex is seen clearly through the large concentration of CO. Since CO is mainly produced through photolysis in the thermosphere, this high concentration must come from large scale descent in the winter mesosphere, which is consistent with the general circulation in figure 2.2. Figure 2.5b shows the distribution of CO measured from the radiometer

at Onsala Space Observatory. The same large scale decent is clearly seen in the concentration of CO during the winter months. Measuring this decent is interesting, as it can be used to test the gravity wave parameterisation of climate models (e.g. Forkman et al. (2003b)).

2.3.2 Ozone chemistry

Chapman Theory

Ozone chemistry in the middle atmosphere was first explained by Sydney Chapman in 1930 (Andrews, 2000). He stated that in the middle atmosphere ozone is created by the combination of molecular oxygen and atomic oxygen



where M is a third body necessary to conserve energy and momentum in the reaction. The source of the atomic oxygen is the photolysis of molecular oxygen by ultra-violet photons with wavelengths less than 240 nm



Ozone is destroyed either by combination with atomic oxygen



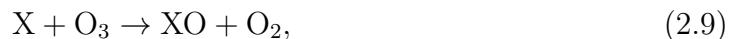
or through the photolysis by photons with wavelengths shorter than 1140 nm



With these reactions, and assuming that reaction 2.8 is much faster than 2.7, the existence of a stratospheric ozone layer can be explained. However, Chapman theory over-predicts the amount of ozone in the lower stratosphere, and neglects transport of odd oxygen which is important to explain how ozone is distributed across the middle atmosphere.

Catalytic Cycles

An important modification to Chapman theory is to take into account ozone destroying catalytic cycles. These are chemical cycles where a catalytic species (X) reacts with ozone in a set of reactions



which have the net effect of removing ozone from the atmosphere, without actually depleting the catalytic species causing the reaction. Examples of important catalytic species in the middle atmosphere are Chlorine (Cl), Hydroxyl (OH) and Nitric Oxide (NO). In the upper stratosphere and mesosphere the reactions involving the hydroxyl radical are the most important.

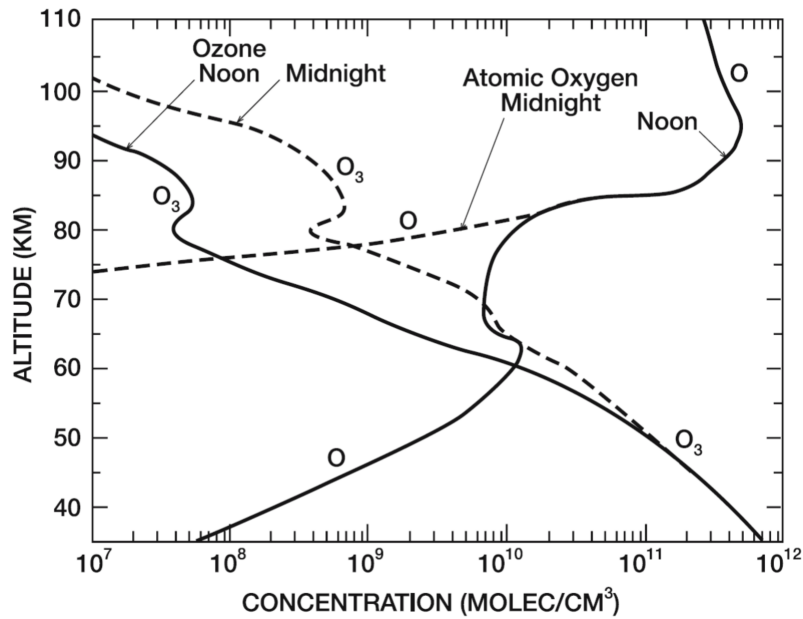


Figure 2.6: Vertical distribution of ozone and atomic oxygen (Brasseur and Solomon, 2005).

Mesospheric Ozone

The ozone distribution in the mesosphere has a large diurnal variation. Figure 2.6 shows the midday and midnight concentration of atomic oxygen and ozone across the mesosphere. During day the photolytic destruction of ozone results in more atomic oxygen compared to ozone. After the sun sets the atomic oxygen is converted into ozone resulting in a general increase of mesospheric ozone during night time.

The local maximum of ozone seen between 80 and 90 km in figure 2.6 is called the “secondary maximum” (the stratospheric ozone layer being the first one). It arises since the production of atomic oxygen reaches a local maximum at these altitudes due to photolysis of molecular oxygen by incoming radiation in the Schumann-Runge continuum and bands (137-200 nm). The secondary maximum is particularly strong during nighttime as the excess atomic oxygen is converted into ozone.

In addition to the two local maxima seen in figure 2.6, a third, “tertiary maximum” of ozone can be found during nighttime at around 72 km at latitudes just equatorwards of the polar night terminator (Marsh et al., 2001). During the polar night the production of hydroxyl (reaction 2.12) is limited due to the lack of solar radiation. However, just at the terminator, UV radiation still penetrates far enough down to produce atomic oxygen, thus a local maximum will arise since the destruction of ozone is lower and production is higher than the areas around it.

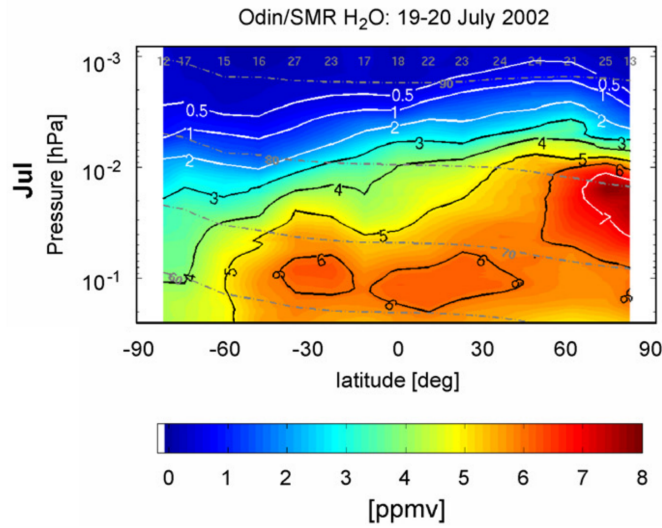


Figure 2.7: Zonal mean mesospheric water vapour from Odin-SMR in July 2002 (Urban et al., 2007).

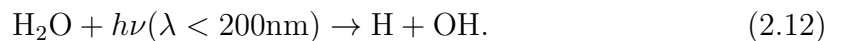
2.3.3 Water vapour chemistry

Water vapour exists in large quantities in the troposphere where evaporation from the Earth’s oceans constantly resupply the atmosphere. However, only a small portion of this water will ever reach the middle atmosphere. The reason for this is that water vapour reaches the middle atmosphere through the tropical tropopause. This region is very cold (190-200 K) and thus most of the water will “freeze dry” out of the air, and only a small fraction, around 3.5-4 ppmv actually enters the stratosphere (Kley and Russell III, 2001).

Once in the stratosphere, water vapour has a long lifetime and is transported polewards by the Brewer-Dobson circulation, and due to its long lifetime (months to years) it can be used as a tracer for stratospheric dynamics. In the stratosphere and lower mesosphere the main sink of water vapour is the reaction



where $\text{O}(^1D)$ implies that the oxygen atom is in an excited state. At higher altitudes the photolysis of water vapour by UV-light into hydroxyl becomes important



The main local source of water vapour in the middle atmosphere is the oxidation of methane (Brasseur and Solomon, 2005). The net result of these reactions is a maximum of water vapour around the stratopause, after which the water vapour concentration drops off with altitude.

Figure 2.7 shows the global distribution of water vapour in the mesosphere measured by Odin-SMR. The local maximum of around 6 ppmv at the stratopause is

seen in the tropical and sub-tropical latitudes, but at the winter and summer pole a strong deviation from this can be seen. At the winter pole (-90°) the strong downwelling inside the polar vortex due to the meridional circulation significantly reduces the amount of water vapour in the mesosphere. In the summer region the general upwelling results in an increase of water vapour in the upper mesosphere. This is further modified by the presence of polar mesospheric clouds (see section 2.2), which redistribute the water through sedimentation and sublimation and can result in local water vapour concentrations far above what is predicted by the simple explanations given by a pure photochemical analysis.

2.4 The Changing Middle Atmosphere

Human influence on the atmosphere has been unequivocally established by scientists throughout the 20th century, but the full implications of these changes are far from understood. For the middle atmosphere, two anthropogenically generated effects are particularly important. The first is the ozone loss in the middle atmosphere resulting from the release of chlorofluorocarbons (CFC). The second phenomenon is the atmospheric change occurring due to the anthropogenic release of greenhouse gases, in particular CO_2 and CH_4 . Understanding these changes, and detecting the possible influences these may have on the middle atmosphere is one of the main motivations for conducting measurements of the mesosphere.

2.4.1 Ozone Loss

Ozone is important for the middle atmosphere as it absorbs UV-radiation, thus heating the middle atmosphere. In the seventies theoretical studies suggested that the amount of ozone in the middle atmosphere could be reduced by anthropogenic release of chlorofluorocarbons (CFCs) (Stolarski and Cicerone, 1974; Molina and Rowland, 1974). Due to their long photochemical lifetime, CFCs can be transported out of the troposphere and into the stratosphere. In the stratosphere they undergo photolysis, and release chlorine, resulting in the destruction of ozone through the catalytic reactions described in section 2.3.2.

The next breakthrough raising concerns about the stratospheric ozone layer was the discovery of the Antarctic ozone hole, by Farman et al. (1985), when a particularly large depletion was seen above Halley bay during early spring. This depletion was much larger than expected by the contemporary models, and in fact so surprising that it was filtered out as “erroneous data” in measurements performed by the Nimbus-7 satellite, and only after reprocessing the data a clear depletion could be found in the satellite data as well (Grundmann, 2001). After this discovery, intense modelling and measurement efforts were undertaken, and by including amongst other, heterogeneous chemistry on Polar Stratospheric Clouds (also called mother-of-pearl clouds) a chemical foundation was established by the late 1980s.

At about the same time, political actions on limiting CFC emissions were under

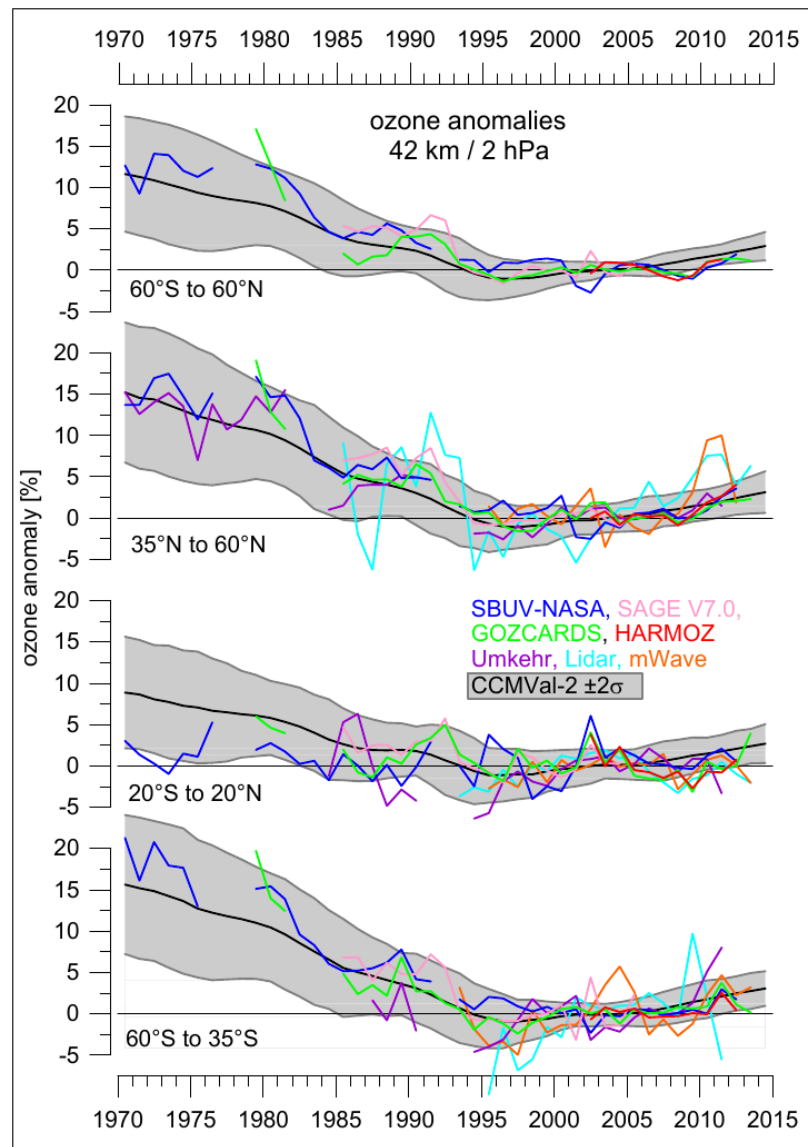


Figure 2.8: Ozone anomalies (compared to the 1998-2008 baseline) from different instruments (coloured) and the CCMVal-2 model (black) at different latitude bands. The grey area indicate ± 2 standard-deviation range for the model annual mean (Pawson et al., 2014).

way. Starting in the late 70s single countries started to ban the use of CFCs as an aerosol propellant, and in 1987 the Montréal protocol was established in which the signing countries promised to phase out production of CFCs and other ozone depleting substances. This limitation has in many ways been successful, and a recovery is seen in the stratospheric ozone concentration since the beginning of this century (Jones et al., 2009). Figure 2.8 shows this recovery and it is expected that a complete recovery will be reached by the middle of the century (WMO, 2014). However, events such as volcanic eruptions, increasing levels of bromine substances, the effects of global climate change and consequences of possible geo-engineering policies may modify and disrupt this recovery. Thus a continued monitoring of the middle atmospheric ozone is important to be able understand the effect of the different drivers of ozone depletion, and in return the effect that ozone depletion (and recovery) might have on the atmosphere as a whole.

2.4.2 Mesospheric Cooling

Greenhouse gases² have their name from the fact that they heat the troposphere since they allow shortwave radiation in the form of UV- or visible light to reach the ground, but trap the re-emitted long wave radiation. The warming effect of greenhouse gases is well known, but they have the opposite, cooling, effect in the middle atmosphere. This cooling occurs since, unlike the lower atmosphere, the main source of heat in the middle atmosphere is the direct absorption of short wave radiation. This mean that an increase in greenhouse gases will not significantly increase the heating at these altitudes, but it will however increase the cooling to space resulting in a temperature decrease (Pierrehumbert, 2010).

The cooling of the middle atmosphere is important as it helps us differentiate between natural and anthropogenic forces on the climate system (Thompson et al., 2012). Cooling of the middle atmosphere has been determined to be ~ 0.5 K/decade in the stratosphere (Thompson et al., 2012) and 1-3 K/decade in the mesosphere (Beig, 2011). However, there is much uncertainty related to how these temperature changes might affect the dynamics in the middle atmosphere, and if any changes in the dynamics will feed back into tropospheric weather patterns.

One puzzling fact is that even though the rest of the middle and upper atmosphere is cooling, a large number of studies assessing the mesopause region show no apparent trend (Beig et al., 2003). And although newer data indicate a weak cooling trend in the mesopause, this trend might not be constant in time, and may even depend on season or month (Offermann et al., 2010). Thus even though trend estimates from model and measurements have become more consistent, many uncertain factors still remain, in particular in assessing the role of dynamical changes, and how gravity wave propagation should be parameterised in the models (Beig, 2011).

Other unresolved questions include how the increased amount of methane in the

²The name greenhouse gas is actually a misnomer as a greenhouse is not mainly heated by the trapping of radiation, but rather by preventing the warm air from escaping.

atmosphere will affect water vapour concentrations in the mesosphere. It is assumed that since photolysis of methane is a major source of water vapour in the mesosphere the concentration will increase. This has of course major implications for polar mesospheric clouds, since their formation is governed by the water vapour available and the mesopause temperature. This increase of clouds would clearly indicate that humans affect the climate not only in the troposphere, but across the entire middle atmosphere. Since the existence of polar mesospheric clouds was first confirmed in 1885, it has been suggested that these clouds did not exist before the industrial revolution (Gadsden, 1982; Schröder, 1999; Butler, 2006), and that they in fact are an early indication of climate change (Thomas, 1996), hence the “miners canary” analogy introduced in section 1.

The debate over the nature of polar mesospheric clouds and their nature have been going on for over two decades (von Zahn, 2003; Thomas et al., 2003), and in particular whether there is any observed trend in their brightness and/or occurrence rate, with different studies showing different results (e.g. DeLand et al. (2007); Kirkwood et al. (2008); Shettle et al. (2009); Hervig and Stevens (2014)). An important question is then: “To what degree is the cloud formation determined by temperature or water vapour concentration, and how will changes (or lack thereof) in these affect the clouds.” To be able to answer these questions, and figure out whether PMCs truly are the “miners canary” of climate change, it is therefore important to obtain good measurements, not only of the clouds, but their surrounding atmosphere as well.

Measurement Principles

To perform remote sensing measurements we need to understand how electromagnetic (EM) radiation arises and propagates through the atmosphere. Furthermore, we need methods that can extract the desired information from the received EM-radiation and understand the errors associated with such methods. This chapter will provide a short introduction to the principles of the remote sensing techniques used in this thesis, and the basic theory needed to understand the errors and uncertainties in such measurements.

3.1 Blackbody radiation

Electromagnetic radiation is radiation arising from fluctuations in electromagnetic fields. It is classified based on its wavelength, and figure 3.1 shows an overview of the EM spectrum. Different categories include the UV- (100 nm to 400 nm), the visible- (400 nm to 700 nm) and the microwave region (mm-cm). The amount of radiation travelling through an area from within a certain solid angle is called radiance and is a useful quantity when discussing the strength of EM-radiation.

A blackbody is an object that absorbs all incident radiation. For such objects the emitted radiance per frequency, L_ν , also called the spectral radiance, is given by Planck's law of radiation

$$L_\nu = \frac{2h\nu^3}{c^2(e^{h\nu/k_bT} - 1)} \left[\frac{\text{W}}{\text{m}^2 \text{Hz sr}} \right]. \quad (3.1)$$

Here h is Planck's constant, ν the frequency of the radiation, c the speed of light, k_b Boltzmann constant and T the temperature of the object.

Not all objects are perfect blackbodies, and to take this into account, thermal radiation from such non-blackbody objects is described by the emissivity. The emissivity, $\epsilon(\nu)$, relates the blackbody spectral radiance to the true spectral radiance by

$$L_\nu = \epsilon(\nu)B_\nu, \quad (3.2)$$

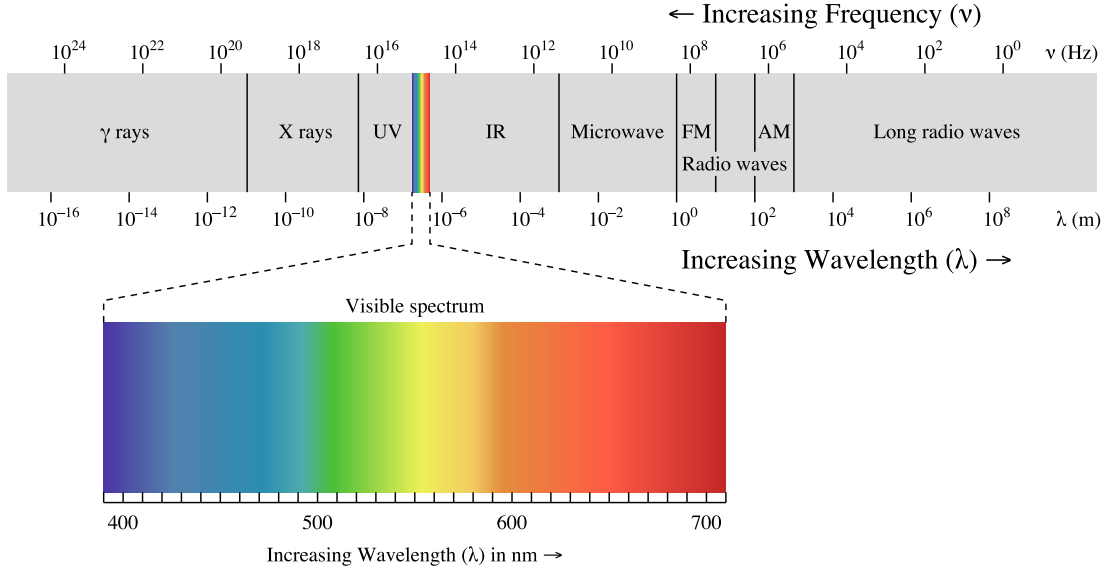


Figure 3.1: The electromagnetic spectrum (Ronan, 2007).

where B_ν is the radiance from a blackbody at the same temperature.

The absorptivity, α , describes how well an object absorbs EM radiation. For a gas in local thermodynamic equilibrium (LTE) Kirchoff's law applies. It states that the absorptivity is equal to the emissivity

$$\alpha = \epsilon. \quad (3.3)$$

Local thermodynamic equilibrium is reached when the rate of collisions between molecules is much higher than the rate of which molecules spontaneously absorb and emit photons, and for most rotational transitions, LTE is valid for the entire middle atmosphere (Lopez-Puertas and Taylor, 2001).

In remote sensing, spectral radiance is usually given in terms of brightness temperature, which is the temperature a blackbody object would need to have in order to radiate with the measured spectral radiance. Thus from equation 3.1 and 3.2 the brightness temperature, T_b can be written as

$$T_b = \frac{h\nu}{k_b} \frac{1}{\ln\left(1 + \frac{1}{\epsilon} (e^{h\nu/k_b T} - 1)\right)}, \quad (3.4)$$

where once again T is the physical temperature of the gas. This nomenclature is particularly useful in the long wavelength-, or Rayleigh-Jeans, approximation ($h\nu \ll k_b T$) where the relationship between the physical temperature and the brightness temperature reduces to

$$T_b = \epsilon(\nu)T. \quad (3.5)$$

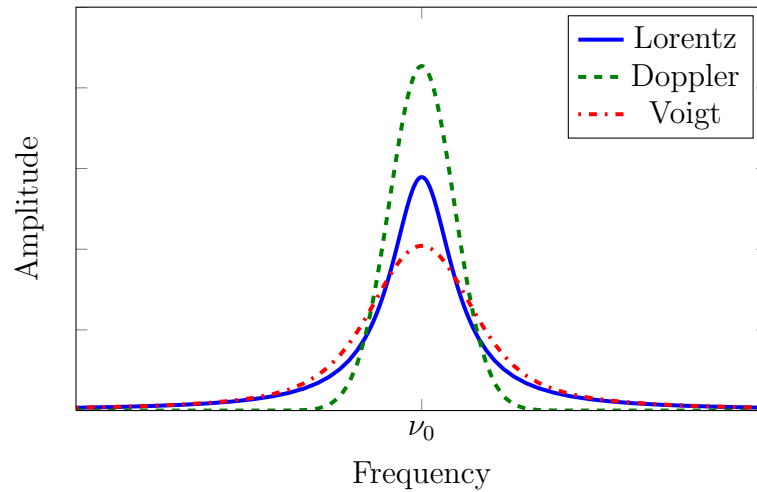


Figure 3.2: Three different line functions describing molecular absorption and emission. The functions are normalised to have the same area under the curve.

3.2 Absorption and emission by gases

Electromagnetic waves travelling through a medium can interact with it. This interaction includes scattering by particles and molecules, where new waves are generated, as well as absorption, where the energy is converted into internal energy of the molecule. For bound changes in internal energy, e.g. electronic, vibrational or rotational transitions, the internal energy change, ΔE , will be related to the absorbed or emitted frequency by

$$\Delta E = h\nu. \quad (3.6)$$

For gases in the atmosphere these energy transitions are affected by line-broadening processes. To describe these processes we introduce the *shape function*, Φ , and the line-strength, S , such that the absorption coefficient for a given molecular transition, i , in a medium is given by

$$\gamma_{abs}^i = n^i S^i \Phi^i(\nu) \left[\frac{1}{\text{m}} \right], \quad (3.7)$$

where n^i is the number density of the corresponding molecule in the medium. The absorption coefficient gives the amount of absorption per unit distance.

Molecules in a gas have a certain velocity relative to the incoming or outgoing EM-wave. This motion leads to a Doppler shift in the absorption/emission frequency. For a given temperature the random velocities of molecules are given by the Maxwell-Boltzmann distribution, and the resulting shape function is a Gaussian (green-dashed line in figure 3.2). The Lorentz line function (blue line in figure 3.2) describes the pressure broadening, which arises due to collisions between molecules. Quantum mechanical states also have an intrinsic lifetime due to the natural decay process. This leads to broadening of the line called natural line broadening. This broadening is

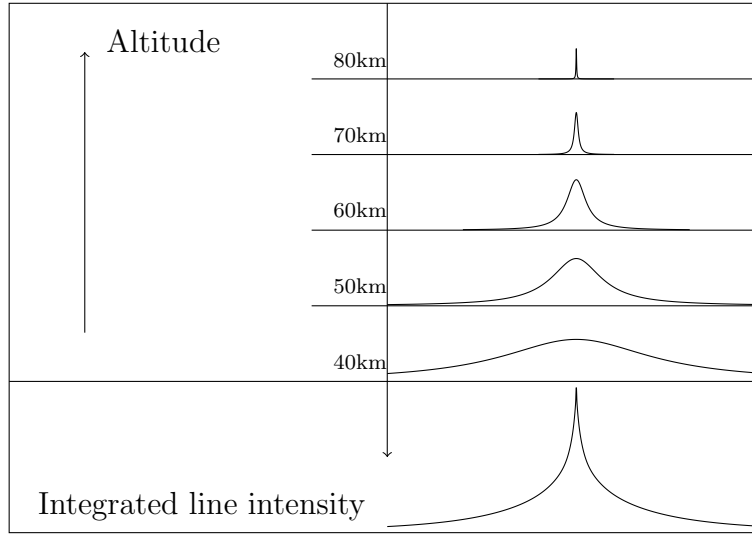


Figure 3.3: An illustration of the radiative transfer equation for an optically thin line. The emission at each altitude is given by the Lorentz function and the total radiation reaching the ground is the sum of the emission at all altitudes.

also described by the Lorentz function, but for transitions in LTE the collisional lifetime is much shorter than the natural lifetime, and natural line-broadening becomes negligible.

In the lower atmosphere, the line-width of a transition will be totally dominated by pressure-broadening as the high density leads to frequent collisions between molecules. As the pressure decreases with altitude, the collisional frequency decreases and the line becomes narrower. At some point the pressure broadened linewidth will become smaller than that of the Doppler broadening, and the spectrum will start to look more Gaussian in shape. At this altitude the clear relationship between lineshape and altitude vanishes since the Doppler width is only dependent on the square root of the temperature, and not the pressure. At altitudes where both pressure and Doppler broadening is important the shape function will take on the Voigt lineshape (red-dot-dashed line). This is a Lorentzian shape convolved with a Gaussian. The Voigt lineshape gives a more realistic description of a line transition in the true atmosphere than using the Lorentzian or Gaussian alone. Other lineshapes also (e.g Vleck-Weisskopf) exists that take into account the more subtle effects of interaction in collisions.

3.3 The radiative transfer equation

The radiative transfer equation describes how EM-energy is transferred along a path s in the atmosphere

$$\frac{dL_\nu}{ds} = -L_\nu\gamma + J_\nu. \quad (3.8)$$

The first term on the right hand side describes extinction, where γ is the extinction coefficient. The second term, J_ν , describes additional sources of radiation along the path. The most common reasons for extinction in the atmosphere are scattering, and absorption along the path of the radiation. Common sources include scattering into the path, and thermal radiation emitted from the atmosphere along the path.

The spectral radiance measured by a microwave detector can be found by integrating equation 3.8 along the line of sight of the instrument. At microwave frequencies scattering can often be neglected (Clancy and Muhleman, 1993), and assuming LTE, the radiative transfer is given by

$$L_\nu(s_{instr}) = L_\nu(s_0)e^{-\tau(s_0,\nu)} + \int_{s_0}^{s_{instr}} \epsilon(s,\nu)B_\nu(T(s))e^{-\tau(s,\nu)} ds, \quad (3.9)$$

where s_0 is the top of the atmosphere, s_{instr} the position of the instrument, and τ is the optical thickness along the path. Neglecting scattering, τ is given by

$$\tau(s) = \int_s^{s_{instr}} \gamma_{abs}(s',\nu)ds', \quad (3.10)$$

where s' indicates integration along the propagation path and γ_{abs} the total absorption coefficient from all molecules and particles along the path. The background source term, $L_\nu(s_0)$, is the incoming radiation at the top of the atmosphere, i.e. the cosmic background radiation. Figure 3.3 illustrates the concept of integrating the radiative transfer equation from the top of the atmosphere for a single, optically thin (i.e. $\tau \ll 1$), transition line measured by a ground-based radiometer. Each altitude contributes with some radiation, and the total measured radiation at ground level is given by the sum of the emitted radiation from each altitude.

A radiative transfer simulator is a computer program that calculates the radiative transfer by solving the radiative transfer equation numerically. The radiative transfer-, or forward, model used in this thesis is the Atmospheric Radiative Transfer Simulator (ARTS) 2 (Eriksson et al., 2011). This is a radiative transfer model developed for the microwave region, and can simulate many different viewing geometries and instruments.

3.4 1-D retrievals

The fact that the shape of absorption and emission lines change with altitude (see figure 3.3) means that a measured spectrum at ground level will not only contain information about the total integrated column of a molecule, but also its altitude distribution. The green and blue lines in figure 3.4a are two altitudes profiles of water vapour which only differ in the mesosphere. The corresponding lines in figure 3.4b show the simulated spectral intensity resulting from these two profiles around

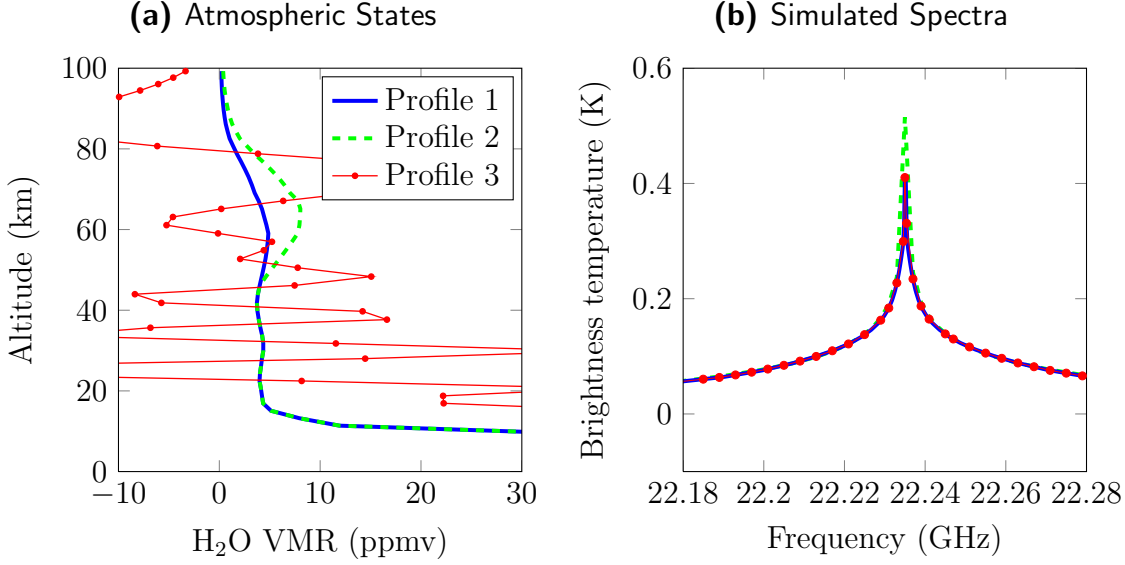


Figure 3.4: Left panel: Some atmospheric water vapour profiles. Profile 1 and 2 represent realistic profiles, while Profile 3 is an example of an unrealistic profile. Right panel: Spectra measured from ground level (ignoring the troposphere and cosmic background radiation) resulting from the different profiles. Note how the unrealistic profile still produces a realistic spectrum similar to the blue profile.

the 22 GHz water vapour transition as measured by an instrument at the ground level (ignoring the troposphere and cosmic background radiation). In the wings the two spectra have the same value, but at the line centre the green spectrum shows a clear increase in brightness temperature. This increase comes from the increased H_2O concentration around 60 km. The increase is only seen at the line centre as the emitted radiation at high altitudes is less affected by pressure broadening than radiation emitted at lower altitudes. This example indicates how we can use the shape and intensity of a line to determine the altitude profile.

The process of determining the true atmospheric profile from a measured spectrum is known as an inversion, or retrieval. To solve this problem numerically on a computer, the radiative transfer equation is discretised and linearised around some atmospheric state. Expressed in linear algebra equation 3.9 becomes

$$\mathbf{y} = \mathbf{K}\mathbf{x} + \epsilon, \quad (3.11)$$

where \mathbf{y} is the measured spectrum arising from from atmospheric state, \mathbf{x} , and with errors, ϵ . $\mathbf{K} \equiv \partial\mathbf{y}/\partial\mathbf{x}$ is the linearised forward model known as the Weighting function- or Jacobian matrix. The vector spaces spanned by \mathbf{x} and \mathbf{y} are called the measurement and state space respectively, and \mathbf{K} can be seen as a mapping from one space to the other. In ARTS 2 the linearisation can be done analytically or numerically (by a finite difference method), while the discretisation is performed assuming a spherical coordinate system with pressure as the altitude coordinate. Furthermore, tri-linear

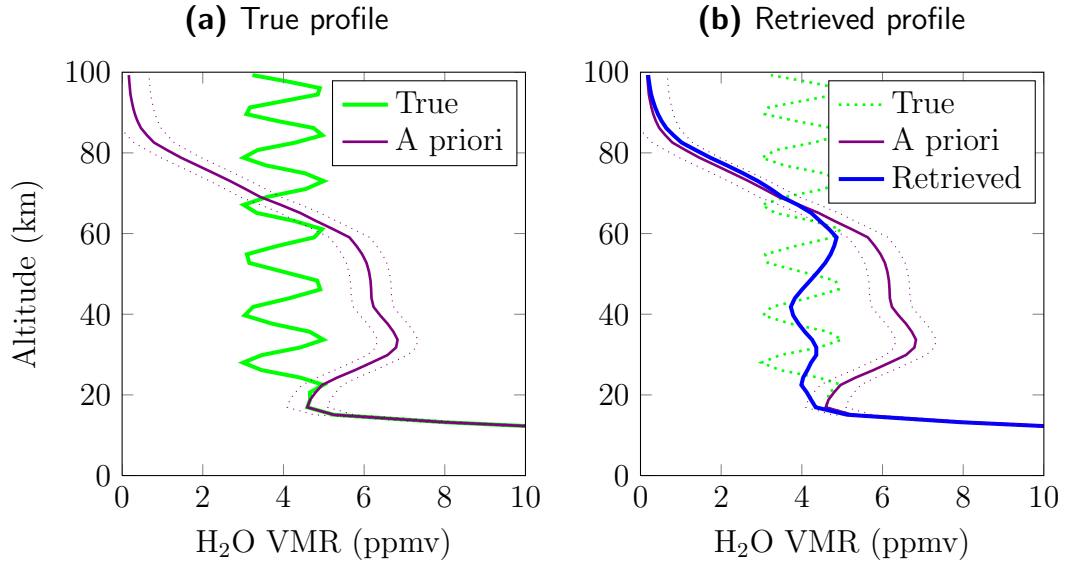


Figure 3.5: A simulated retrieval of water vapour. The true profile (green-solid and green-dotted lines), the a priori profile (violet lines) and the a priori standard deviation (dotted-violet lines). In absence of noise, the retrieved state (blue line) ends up as a smoothed version of the true profile.

interpolation (for 3D-atmospheres) is used to estimate the values of the atmospheric fields between grid points.

Naively one might think that finding \mathbf{x} for a given \mathbf{y} could be solved by inverting \mathbf{K} , or using a least squares method to estimate \mathbf{x} . However, the problem of retrieving \mathbf{x} is usually ill-posed. Formally this is due to \mathbf{K} being rank-deficient. Physically this means that there is not a unique profile that reproduces the measured spectrum. This is illustrated by the red dotted lines in figure 3.4a and 3.4b. The red profile of water vapour looks very different from the blue profile. However, when the spectrum resulting from this profile is calculated, it will be exactly equal to that resulting from the blue profile. This means that if an instrument measures a radiance corresponding to the blue spectrum in figure 3.4b, it is formally impossible to determine whether the true atmosphere looks like the red or the blue profile in figure 3.4a.

It is possible to mitigate this problem of non-uniqueness. By inspection we can actually see that the red profile is unphysical as it contains negative concentrations of H_2O . Furthermore, based on the current knowledge of atmospheric chemistry and dynamics, we know that the large fluctuations seen in H_2O , would not exist in the atmosphere. Thus, by inspection it is possible to determine that the blue profile in figure 3.4a is the more probable solution to the inverse problem. Such a restriction of possible solutions is called a regularisation method.

A common regularisation method used for microwave spectrometers is the maximum a posteriori (MAP) method, also called the optimal estimation method (Rodgers, 2000). This method uses a statistical description of the expected profile to constrain

the retrieved values. It is based on the Bayesian approach of estimating probability distributions. In statistical terms, the inverse problem presented can be posed as: “What is the probability of an atmospheric state \mathbf{x} to exist given the measurement \mathbf{y} ”. Applying Bayes’ theorem, the solution can be expressed as:

$$p(\mathbf{x}|\mathbf{y}) = \frac{p(\mathbf{x})p(\mathbf{y}|\mathbf{x})}{p(\mathbf{y})}, \quad (3.12)$$

where p is the probability density function of the respective variables. The important detail in this equation, with regards to the MAP method, is the fact that the a posteriori distribution, $p(\mathbf{x}|\mathbf{y})$, depends on the probability of the existence of state \mathbf{x} , $p(\mathbf{x})$, called the a priori distribution. Hence, for the inverse problem shown in figure 3.4a, the red profile would be regarded as “improbable”, i.e. $p(\mathbf{x}) \approx 0$, resulting in an a posteriori probability for this profile close to zero. The most probable state, given both the measurement and the a priori information, is the maximum of the a posteriori probability density function, and this is regarded as the retrieved profile from the MAP method (hence its name¹).

If $p(\mathbf{x})$ is given by a normal distribution, it can be expressed by an expectation value \mathbf{x}_a and a covariance matrix \mathbf{S}_a . A covariance matrix is a matrix which for a set of stochastic variables has elements $\mathbf{S}_{ij} = \sigma_i\sigma_j\rho_{ij}$, where ρ_{ij} is the correlation between variable i and j , and σ_i and σ_j are their respective standard deviations. Thus, \mathbf{S}_a describes the uncertainty in the a priori profile. The larger the uncertainty in the a priori profile, the less constraint is placed on the retrievals. Figure 3.5 shows a simulated retrieval of water vapour in the middle atmosphere. The green line shows the true profile. The blue line in 3.5b is the profile retrieved using the violet line as the a priori constraint. The standard deviation of the a priori profile is shown as the dotted-violet line.

To use the a priori profile as a constraint, a cost function, χ^2 , is defined. This function describes how well the retrieved state, $\hat{\mathbf{x}}$, fits the measured spectrum ($\mathbf{y} - \mathbf{K}\hat{\mathbf{x}}$), and how well it fits the a priori profile ($\hat{\mathbf{x}} - \mathbf{x}_a$). Scaling the two fitting parameters with their uncertainty gives

$$\chi^2 = (\hat{\mathbf{x}} - \mathbf{x}_a)^T \mathbf{S}_a^{-1} (\hat{\mathbf{x}} - \mathbf{x}_a) + (\mathbf{y} - \mathbf{K}\hat{\mathbf{x}})^T \mathbf{S}_\epsilon^{-1} (\mathbf{y} - \mathbf{K}\hat{\mathbf{x}}), \quad (3.13)$$

where \mathbf{S}_a and \mathbf{S}_ϵ are the covariance matrices describing the uncertainty in the a priori profile and the measurement vector, respectively.

To find the minimum of the cost function χ^2 , it is helpful to first consider an analogous 1-dimensional case. Two measurements, x_ϵ and x_a , with uncertainties σ_ϵ and σ_a , are performed of the same scalar variable x . The optimal way of combining these to measurements in order to estimate x is to scale each of the measurements with their uncertainties

$$\hat{x} = \left(\frac{1}{\sigma_\epsilon^2} + \frac{1}{\sigma_a^2} \right)^{-1} \left(\frac{x_\epsilon}{\sigma_\epsilon^2} + \frac{x_a}{\sigma_a^2} \right), \quad (3.14)$$

¹Statistical methods that do not use a priori regularisation are often referred to as Maximum likelihood (ML) methods.

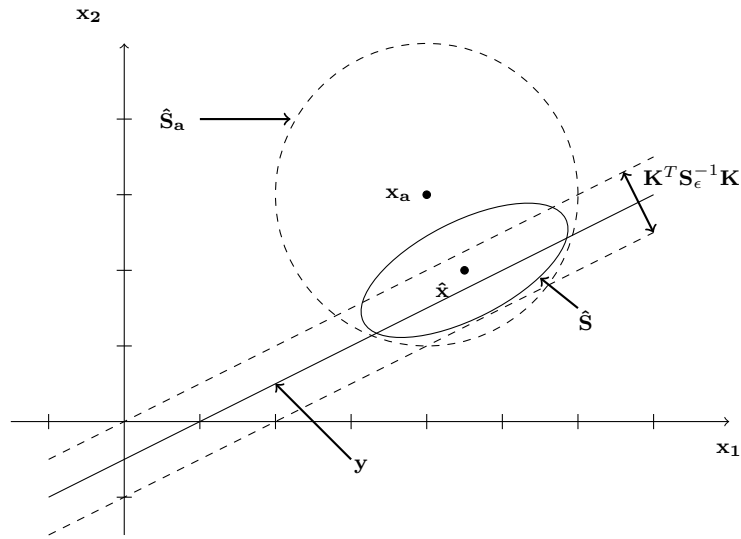


Figure 3.6: A schematic representation of the maximum a posteriori retrieval method. The states corresponding to the measurement, y , gives an ambiguous relationship between the two atmospheric variables x_1 and x_2 . \hat{x} is the value retrieved using the MAP method, and the a priori state is given by x_a . The a priori covariance matrix is given by S_a , the measurement uncertainty mapped to the state space is given by $K^T S_\epsilon K$, and the a posteriori error by \hat{S} . Redrawn from Rodgers (2000).

where \hat{x} is the “optimal” estimate of x based on the two measurements.

Using the matrix formalism introduced earlier, the state minimising χ^2 is given by

$$\hat{x} = (\mathbf{K}^T \mathbf{S}_\epsilon^{-1} \mathbf{K} + \mathbf{S}_a^{-1})^{-1} (\mathbf{K}^T \mathbf{S}_\epsilon^{-1} \mathbf{K} x + \mathbf{S}_a^{-1} x_a) \quad (3.15)$$

The similarities between equation 3.15 and equation 3.14 can be seen. The difference is that in the matrix formulation the scalars in equation 3.14 describing the uncertainties are replaced by covariance matrices. For the a priori profile this is S_a . For the measurement it is the covariance describing errors in the measurement mapped to the state space, $K^T S_\epsilon^{-1} K$.

Figure 3.6 illustrates the concept of MAP geometrically. The inverse problem posed is to find a position in the state space spanned by x_1 and x_2 . A measurement provides some information on the relationship between x_1 and x_2 , but any of the states along the line given by the measurement y is a possible solution. The retrieved state, \hat{x} , is the point which minimises χ^2 , so it is located between x_a and y , where the exact distance from x_a and y is determined by the constraint posed by S_a and S_ϵ .

It should be noted that for the retrieved solution to truly be the “optimal” or maximum a posteriori estimate the covariance matrices used and x_a must be an accurate description of the a priori knowledge about the retrieval problem. This is not always possible. From a practical point, the true statistical state of the atmosphere, in particular the mesosphere, is often unknown, and theoretically sometimes even not

possible to describe with a normal distribution. Furthermore, it is often desirable to ensure that any atmospheric signal sought after in the measurements is not contaminated by the a priori information. These signals can include seasonal variations, wave structures or other atmospheric variations which in theory could be included in the a priori information, but are consciously not included in order to simplify the analysis of the retrieved data. Thus the a priori constraints can to some degree be considered tunable parameters which depend on the practical implementation of the retrieval problem. Hence, although the term MAP or optimal estimation is used in this thesis to describe the regularisation scheme used, it does not necessarily imply that the resulting solution is the optimal in statistical terms.

3.5 Limitations of an retrieval

The MAP method does not only provide a retrieved profile, but can also be used to estimate the error in the retrieved profile. Following Rodgers (2000), equation 3.15 can be written as

$$\hat{\mathbf{x}} = \mathbf{x}_a + \mathbf{G}(\mathbf{y} - \mathbf{K}\mathbf{x}_a), \quad (3.16)$$

where \mathbf{G} is the gain-matrix

$$\mathbf{G} \equiv \partial\hat{\mathbf{x}}/\partial\mathbf{y} = (\mathbf{K}^T\mathbf{S}_\epsilon^{-1}\mathbf{K} + \mathbf{S}_a^{-1})^{-1}\mathbf{K}^T\mathbf{S}_\epsilon^{-1}. \quad (3.17)$$

Using equation 3.11 and 3.16, the error in the retrieval, $\hat{\mathbf{x}} - \mathbf{x}$, can now be calculated through

$$\begin{aligned} \hat{\mathbf{x}} - \mathbf{x} &= \mathbf{x}_a + \mathbf{G}(\mathbf{y} - \mathbf{K}\mathbf{x}_a) - \mathbf{x} \\ &= \mathbf{x}_a + \mathbf{G}(\mathbf{K}\mathbf{x} + \epsilon - \mathbf{K}\mathbf{x}_a) - \mathbf{x} \\ &= (\mathbf{G}\mathbf{K} - \mathbf{I})(\mathbf{x} - \mathbf{x}_a) + \mathbf{G}\epsilon. \end{aligned} \quad (3.18)$$

The first term in the last line of equation 3.18 is known as the smoothing error, and represents the error in the retrieved state as a result of the limited resolution of the retrieval. The effect of the limited resolution can be seen in figure 3.5b as the retrieved state (blue line) does not follow the variation of the true state (green dotted line), but rather a smoothed version of these variations. This limited vertical resolution is usually described by the averaging kernel matrix

$$\mathbf{A} \equiv \frac{\partial\hat{\mathbf{x}}}{\partial\mathbf{x}} = \mathbf{G}\mathbf{K}. \quad (3.19)$$

Each element, \mathbf{A}_{ij} , in this matrix describes the change in the retrieved variable $\hat{\mathbf{x}}_i$ from a change in the real atmospheric variable \mathbf{x}_j . Figure 3.7a shows the rows of the averaging kernel matrix from the retrievals depicted in figure 3.5. These rows are called the averaging kernels (AVKs). They indicate which altitudes the retrieved water vapour concentration at each altitude takes information from. The full width at

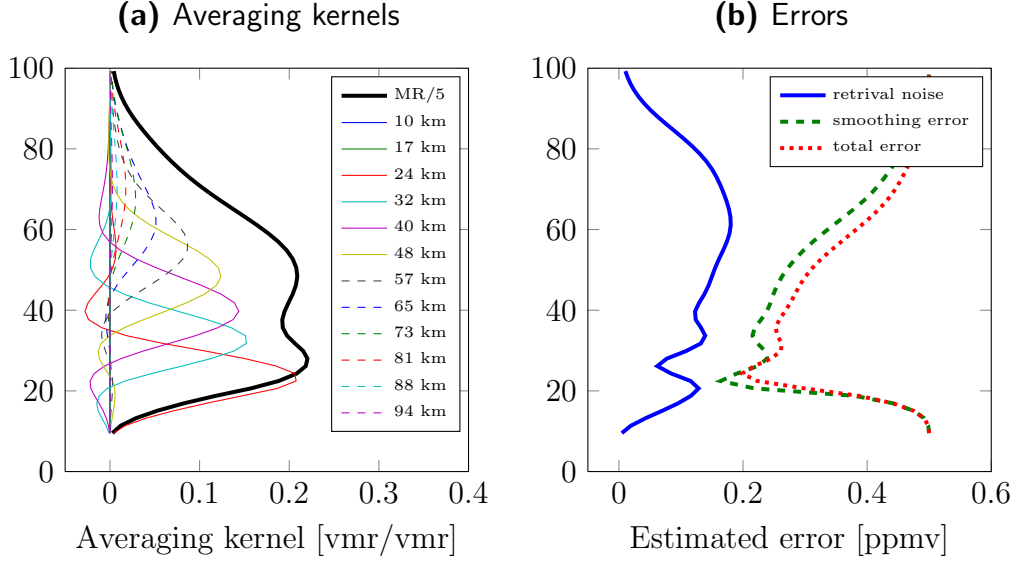


Figure 3.7: Left: Averaging kernels for different altitudes for the retrieval in figure 3.5. The thick black line is the measurement response divided by 5. Right: The square root of the diagonal elements of \mathbf{S}_m (blue solid), \mathbf{S}_s (green dashed) and $\hat{\mathbf{S}}$ (red dotted).

half maximum (FWHM) of these kernels can be considered as a measure of the vertical resolution of the retrievals. Assuming that the covariance of the true atmosphere is correctly described by \mathbf{S}_a the covariance of the smoothing error is

$$\mathbf{S}_s = (\mathbf{A} - \mathbf{I})\mathbf{S}_a(\mathbf{A} - \mathbf{I})^T. \quad (3.20)$$

The area of an averaging kernel gives an indication to what degree the retrieved value at that altitude uses information from the measurement. This value, called the measurement response, is plotted as the solid black line in figure 3.7a. A rule of thumb is that measurement response should be larger than 0.8 for a retrieved value to be considered valid.

The second term in equation 3.18 is the error in the retrievals resulting from errors in the measured spectrum. If the errors in the measured spectrum solely come from thermal noise in the measurement, this second term is called the retrieval noise, and its covariance is given by

$$\mathbf{S}_m = \mathbf{G}\mathbf{S}_\epsilon\mathbf{G}^T. \quad (3.21)$$

Figure 3.7b depicts the square root of the diagonal elements for the different error terms for the retrievals in figure 3.5, including the total estimated retrieval error

$$\hat{\mathbf{S}} = (\mathbf{K}^T\mathbf{S}_\epsilon^{-1}\mathbf{K} + \mathbf{S}_a^{-1})^{-1}. \quad (3.22)$$

To calculate these errors the covariance matrices \mathbf{S}_a and \mathbf{S}_ϵ need to be specified. In the example presented here they are diagonal matrices with diagonal elements of 0.5^2 (ppmv) and 0.05^2 K respectively.

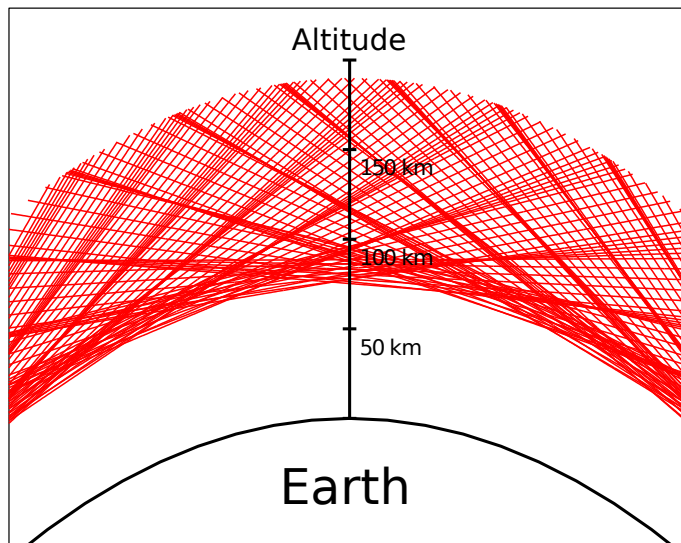


Figure 3.8: Line of sight for tomographic measurements from the Odin satellite. The variation in the distance between the lines occurs due to the satellite scanning both up and down as it orbits around the Earth.

3.6 Multidimensional retrievals

The previous two sections discussed how to retrieve an atmospheric profile from a measurement performed with a ground-based microwave radiometer. Using the formalism developed it is easy to apply this method to limb-sounding instruments, and even extend it to inverting several spectra simultaneously. This chapter will elaborate on how to perform this extension, and how it can be used to perform tomographic retrievals from limb sounding instruments, which are instruments measuring the atmosphere from the side (see section 4.4).

3.6.1 Tomographic measurements

The need for multidimensional retrievals arise when the weighting function of multiple measurements overlap. If the measurements are performed from several different angles the measurements are called tomographic measurements. Figure 3.8 shows the line of sight of the two instruments on the Odin satellite during a set of such measurements. Since the field of view overlaps between measurements (seen by the criss-cross patterns), each measurement contains information relevant for other measurements, and as such, all measurements should ideally be inverted simultaneously.

Such tomographic measurements of the atmosphere has been performed since the 1970s (e.g. Thomas and Donahue (1972)). Algebraic reconstruction techniques (ART) have been used to retrieve airglow in the lower thermosphere (Solomon et al., 1984), and form the basis for the retrieval of the polar mesospheric cloud data used in this thesis (see section 4.4.1). However, for the microwave measurements the the MAP

method as described in the previous sections is used. One advantage of doing this is that the error characterization described in section 3.5 naturally extends into 2-D retrievals. Similar approaches, both with and without a priori regularisation, have previously been developed for and used by limb instruments such as the Michelson Interferometer for Passive Atmospheric Sounding (Carlotti et al., 2001; Steck et al., 2005) and Microwave Limb Sounder (Livesey et al., 2006).

The first step in extending the MAP method into multiple dimensions is to define the measurement vector, \mathbf{y} , as a collection of spectra, rather than a single one. Now depending on whether or not the measurements cover the same or different areas of the atmosphere the state vector might be expanded to not only cover one set of altitude grid points, but a whole collection of them covering different areas (or even different times). The matrices in equation 3.11 then become

$$\mathbf{y} = \begin{pmatrix} y_1^1 \\ \vdots \\ y_m^1 \\ y_1^2 \\ \vdots \\ y_m^2 \\ y_1^3 \\ \vdots \\ y_m^M \end{pmatrix}, \quad \mathbf{K} = \begin{pmatrix} \mathbf{K}_1^1 & \cdots & \mathbf{K}_1^N \\ \vdots & \ddots & \vdots \\ \mathbf{K}_M^1 & \cdots & \mathbf{K}_M^N \end{pmatrix}, \quad \mathbf{x} = \begin{pmatrix} x_1^1 \\ \vdots \\ x_n^1 \\ x_1^2 \\ \vdots \\ x_n^2 \\ x_1^3 \\ \vdots \\ x_n^N \end{pmatrix}, \quad (3.23)$$

where m is the length of a single spectrum, M is the number spectra that are to be inverted, n is the number of altitude grid points for a single profile, and N the number of profiles to be simultaneously retrieved. Naturally the forward model must take into account how changes in the entire atmosphere affects all measurements, and thus \mathbf{K} is an $(m \cdot M) \times (n \cdot N)$ matrix, where each element is the linearised forward model which maps the atmospheric state described by x_i^j to a brightness temperature in a measurement y_l^k . With this rather straightforward expansion equation 3.15 can now be solved for an arbitrary number of measurements and atmospheric grid points.

3.6.2 2-D covariance matrix

Defining the covariance matrices for multidimensional retrievals is a bit more complicated than for the 1-D case. In particular, the covariance between the elements in \mathbf{x} needs to be specified taking into account the correlation in all dimensions. This correlation can be defined using a correlation function, $\rho = \rho(\Delta x, \Delta y, \dots)$, which returns the correlation between two points based on the distance between them in the different dimensions $(\Delta x, \Delta y, \dots)$. Examples of three correlation functions are shown in figure 3.9. The functions are designed such that the correlation length, i.e. distance where the correlation has dropped of by a factor e , is the same for all of them. To convert these functions into two dimensional correlation functions an assumption must be made with regards to the statistical relationship of the variability

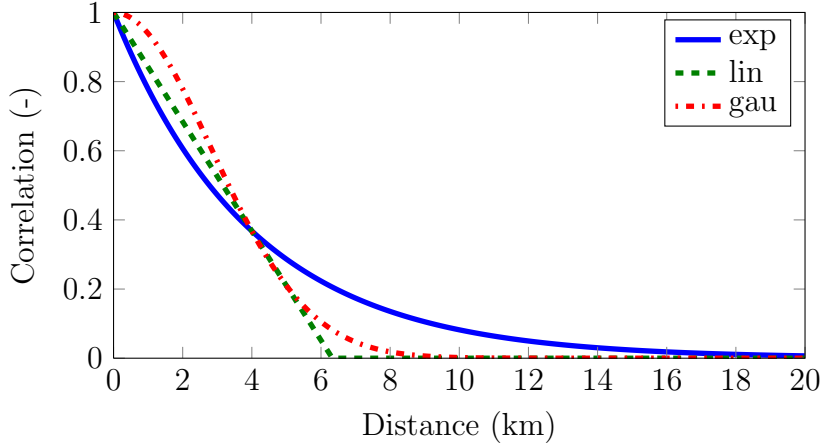


Figure 3.9: 1-D correlation functions describing how an hypothetical atmospheric variable correlates with itself as a function of distance. The three functions describe exponential, linear and Gaussian correlation - all with the same correlation length (4 km).

in the two dimensions. If we assume that the correlation in the two dimensions is separable, i.e. that the total correlation is given as the product of the correlations in each dimension. For two dimensions x, y the correlation then becomes

$$\rho(\Delta x, \Delta y) = \rho_x(\Delta x) \cdot \rho_y(\Delta y), \quad (3.24)$$

where ρ_x and ρ_y are the 1-D correlation functions in each dimension respectively. If, on the other hand, the variability in each dimension cannot be separated, a true multidimensional correlation function must be defined. Defining the correlation length in two dimensions l_x, l_y , the 2-D correlation functions for the three examples in figure 3.9 become:

$$\rho_{exp}(\Delta x, \Delta y) = e^{-\sqrt{(\frac{\Delta x}{l_x})^2 + (\frac{\Delta y}{l_y})^2}}, \quad (3.25a)$$

$$\rho_{lin}(\Delta x, \Delta y) = 1 - 2(1 - e^{-1}) \cdot \sqrt{(\frac{\Delta x}{l_x})^2 + (\frac{\Delta y}{l_y})^2}, \quad (3.25b)$$

$$\rho_{gau}(\Delta x, \Delta y) = e^{-((\frac{\Delta x}{l_x})^2 + (\frac{\Delta y}{l_y})^2)}, \quad (3.25c)$$

To illustrate the differences between a separable and non-separable 2-D correlation function, two examples are shown in figure 3.10 both assuming and not assuming separability. Along the two axes the functions are identical, but along the diagonals they differ significantly. Assuming separability reduces the correlation between two points which are separated in both dimensions.

3.6.3 2-D Averaging kernels and Errors

Expanding the retrieval into two dimensions means that any correlation in the error matrices as well as the resolution estimates discussed in section 3.5 needs to be described in both these dimensions. The averaging kernel for a single retrieval grid point

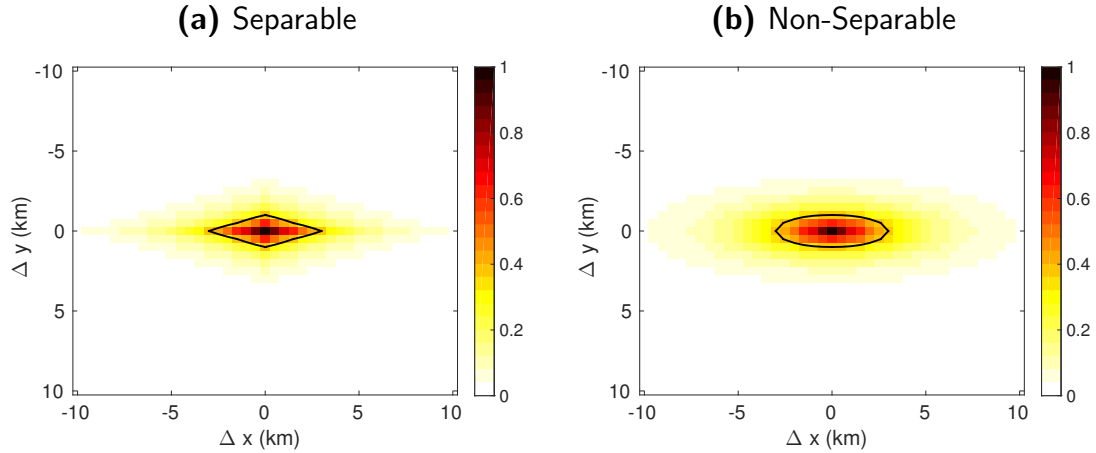


Figure 3.10: 2-D correlation functions assuming an exponential correlation in both dimensions with correlation lengths of 1 and 3 km in the vertical and horizontal direction respectively. The solid black line shows the contour where the correlation has dropped to e . The left panel shows the correlation assuming the variation in the two dimensions is separable, and the right panel shows the correlation without this assumption (equation 3.25a).

located at 80 km from a set of tomographic inversions performed with Odin-SMR is shown in figure 3.11a. Here it can be seen that the retrieved value at the grid point contains information from all points surrounding it, whether they are separated in the vertical or horizontal direction.

For the 1-D averaging kernels shown in figure 3.7a the FWHM of the kernel was regarded as a measure of the vertical resolution of the retrieval. In a similar way the 2-D averaging kernels in figure 3.11a can be separated into a horizontal and a vertical component consisting of the elements along the respective axes. These components can be regarded as the horizontal and vertical averaging kernels for the retrievals, and from this a spatial resolution can be estimated (von Clarmann et al., 2009).

However, using the components along the two axes in the two-dimensional averaging kernel has some pitfalls. In particular this metric ignores the contribution from all points not exactly at the same vertical/horizontal position. It is therefore useful to redefine the horizontal and vertical averaging kernels for tomographic retrievals to the sum of the 2-D averaging kernel over all columns corresponding to a certain vertical or horizontal position. This means that the kernels express the total influence of changes occurring at a different horizontal/vertical position, rather than just the changes of grid points along the two axes.

Figure 3.11b shows the horizontal averaging kernel for the retrieval point marked by the black dot in figure 3.11a calculated using the two definitions. The horizontal AVK calculated using the elements along the horizontal axis has a more jagged structure and even multiple peaks, whereas the AVK calculated using the sum along the vertical axis appears smoother and more similar to the AVKs for the 1-D retrievals.

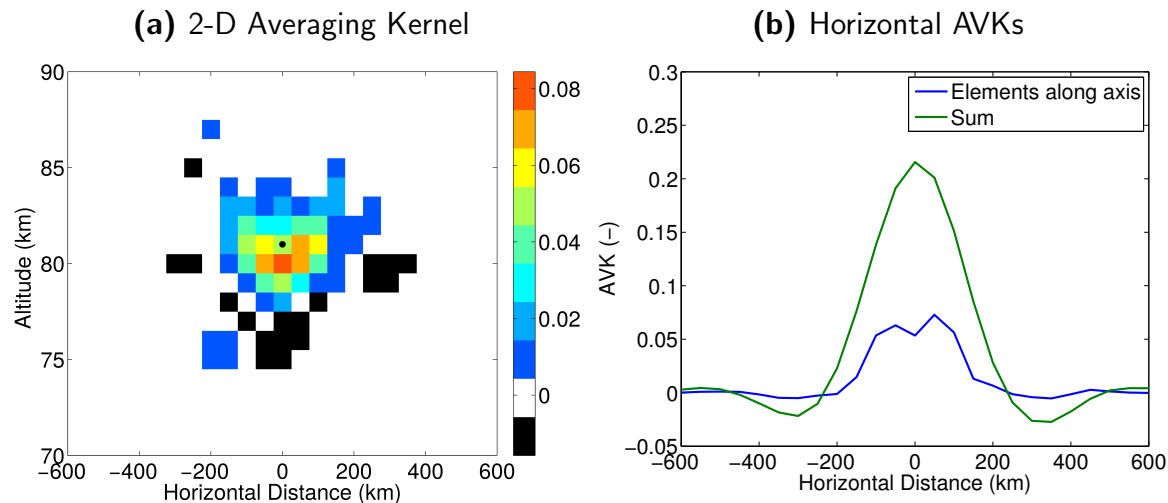


Figure 3.11: Left: A 2-D averaging kernel from tomographic measurements by Odin-SMR. The kernel is plotted for the grid point at 81 km given by the black dot. Right: The horizontal averaging kernel calculated from the same 2-D averaging kernel using either the elements along the horizontal axis (blue line) or the sum of the vertical averaging kernel at each horizontal grid point (green).

The averaging kernel definition used affects the value of the measurement response of the measurements as well. The area under the horizontal averaging kernels defined using the elements along an axis is smaller than the one from the sum of the elements. These two measurement responses are in essence answers to two different questions. The area under the averaging kernel calculated using the elements along axis describes how sensitive the retrievals are to a unit change in the state vector along that particular axis, whereas the area under the summed AVK gives the sensitivity of the retrievals to a unit change of the retrieved variable across the entire retrieval grid and is therefore consistent with the measurement response as defined for 1-D retrievals.

The choice of AVK definition depends on the scientific question asked. For the tomographic measurements in Paper D, the summed version of the AVKs are used, and the measurement response is defined accordingly. In Paper B however, the second dimension for the 2-D retrievals is not space, but time, and since the main goal of the paper is to compare the time-series inversion method described with traditional 1-D retrievals the averaging kernels and measurement response were described using the elements along axis method.

3.7 Instrumental error sources

Estimating errors is an important part of making a measurement, and accurate error estimations are needed to ensure that measurements can be properly compared to each other, and to models. When doing an error analysis it is common to separate

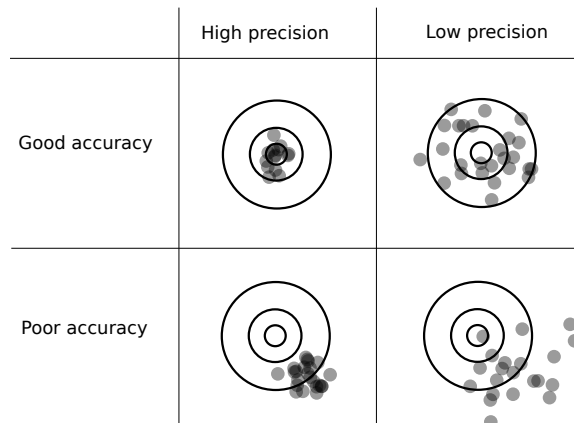


Figure 3.12: The effect of accuracy and precision on a set of measurements (dots). The true value is the bullseye.

errors into random errors and systematic errors. A basic assumption of random errors is that it is possible to decrease them by repeating the same measurement several times, and taking the average. Systematic errors on the other hand, will not be reduced by averaging. Figure 3.12 shows the difference between these error types. The magnitude of the errors are known as precision (random errors) and accuracy (systematic errors).

Random errors are often possible to characterise based on knowledge of the instrument, or by looking at the variability in the measured quantity and compare it to the expected variability. As discussed in the last section, the MAP method can provide an estimate of the expected random errors through the the a posteriori covariance matrix, $\hat{\mathbf{S}}$. The MAP method can also be used to estimate other errors. However, some errors might come from unknown defects in the instrument, and can only be discovered through cross-comparing the results with other instruments.

CHAPTER 4

Instruments

To interpret an atmospheric measurement, it is important to understand the instrument performing the measurement. This chapter will introduce the instruments used in this thesis, starting with an overview of different measurement techniques and geometries. Particular emphasis will be put on the microwave spectrometer, since it has been the main focus of the papers on which this thesis is based.

4.1 Measuring the atmosphere

We all have the ability to make observations of the atmosphere, and we do so every day by looking at clouds or enjoying a beautiful sunset. For detailed atmospheric science, however, a range of sensors and platforms have been developed. When observing the Earth, it is normal to differentiate between two types of measurement techniques. In-situ measurements sample the atmosphere directly at the desired position, whereas in remote sensing, electromagnetic (EM) radiation is used to gather information about the atmosphere, potentially far away from the position of the instrument¹. An overview of some remote sensing instrument platforms is shown in figure 4.1. Each platform has its advantages and disadvantages, and depending on the phenomenon studied, one particular system, or combination of systems, is advantageous.

Ground-based instruments used to study the middle atmosphere include UV-, IR-, and microwave spectrometers, lidars and radars. These are located on the ground and look upwards into the atmosphere. Such instruments are usually cheaper and easier to maintain than similar instruments on other platforms. This means that they have the possibility to continuously measure and monitor the atmosphere above a specific location over long time periods. Their main limitation is that the instruments cover a limited geographic area, compared to air-borne or satellite-borne instruments.

¹These methods are not only used in atmospheric science. For example McNoleg (1996) even suggested to use remote sensing to map the habitat of the fabled highland haggis.

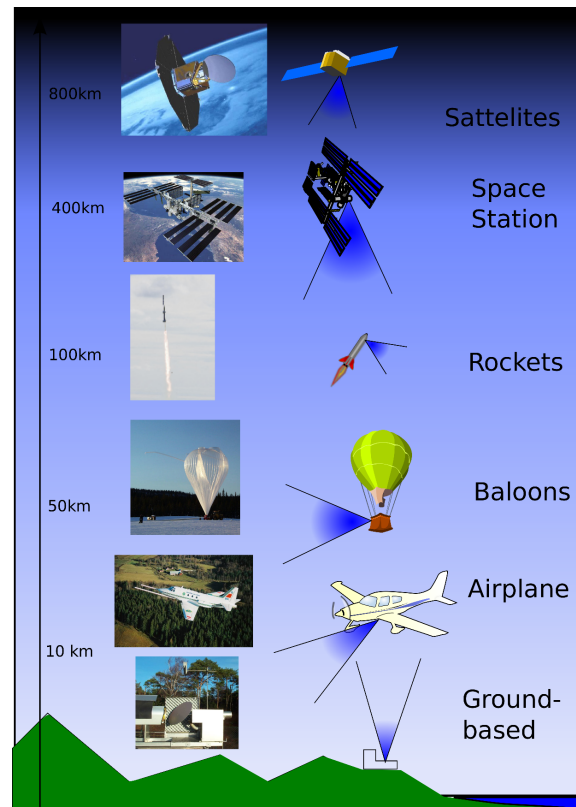


Figure 4.1: Overview of instrument platforms used for studying the atmosphere. The altitudes for the different platforms are approximate.

On the opposite side of the scale are instruments orbiting the planet on space-stations or satellites. These provide the ultimate geographical coverage as they, in principle, can measure the entire globe. In practice however, their geographical coverage is limited by orbit and type of instrument. Satellite-borne instruments that use an orbit designed to give global coverage, will lack in the ability to measure local or short term transient phenomena.

4.2 The microwave spectrometer

Radiometers are instruments that measure the radiance of EM-radiation. Different radiometers exist for the different regions of the EM-spectrum. A particular type of radiometer is the spectrometer which measures the radiance as a function of frequency. Figure 4.2 shows an overview of a heterodyne microwave spectrometer. The radiation from the atmosphere is captured by an antenna. The frequency of the measured atmospheric signal at the antenna is called the radio frequency (RF). After being captured, this signal may be amplified and/or filtered depending the receiver design. The signal is then mixed non-linearly with a signal of known frequency from a local oscillator (LO). By mixing these two signals, the frequency of the radio signal can be

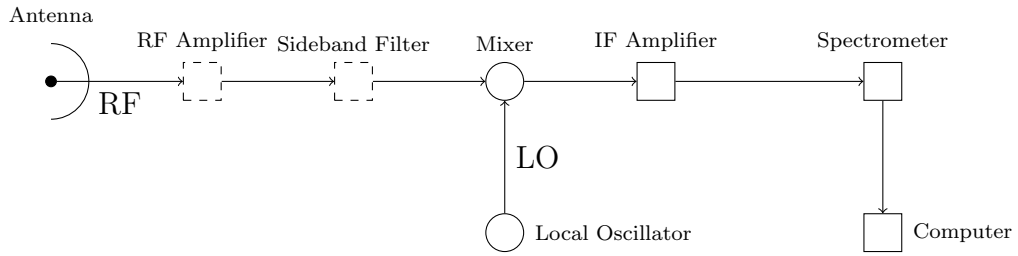


Figure 4.2: A schematic view of a microwave spectrometer.

reduced to a lower intermediate frequency (IF), before it is amplified, sampled and fed to a spectrometer. This downconversion is necessary since high frequency signals are difficult to digitise.

The mixing technique is called heterodyne mixing. It is performed by a non-linear component called a mixer. In its simplest form a mixer can be described as a device with a purely quadratic response (Rohlfis and Wilson, 2008). If the incoming signal is the sum of the LO and RF signal the quadratic signal leaving the mixer is

$$(A \sin(\omega_{RF}t) + B \sin(\omega_{LO}t))^2 = \frac{1}{2}(A^2 + B^2) - \frac{1}{2}A^2 \cos(2\omega_{RF}t) - \frac{1}{2}B^2 \cos(2\omega_{LO}t) + AB \cos(\underbrace{(\omega_{RF} - \omega_{LO})}_{\omega_{IF}}t) - AB \cos((\omega_{RF} + \omega_{LO})t).$$

The intermediate frequency, ω_{IF} , is thus given by the difference between the LO frequency, ω_{LO} , and radio frequency, ω_{RF} . Due to the symmetry of the intermediate frequency term, signals from both $\omega_{LO} + \omega_{IF}$ and $\omega_{LO} - \omega_{IF}$ will be included in the IF signal. Thus, two RF bands are included in the IF signal, one on each side of the LO frequency. Figure 4.3 illustrates the principle of heterodyne detection, and shows the two RF bands. If the frequencies of interest are located in only one of the bands, a sideband filter is usually applied in front of the mixer to filter out the unwanted, or image-band. Such a receiver is called a single sideband receiver. Another option is using both bands, creating a double sideband receiver.

4.2.1 Calibration

Calibration is needed to lend physical meaning to the electrical signal from the detector. Assuming a linear system, this can be done by performing a measurement of thermal radiation from two known sources, or loads, one hot and one cold. This measurement can then be used to determine the relationship between the measured signal, V , and the brightness temperature T_b . These loads can in principle be anything radiating with a known brightness temperature, such as an absorber at ambient temperature. Similarly, the cold load can for example be an absorber cooled by liquid nitrogen or helium. For satellite instruments, looking into black space provides a particular cool cold load. Figure 4.4 shows the calibration procedure. The resulting equation for determining the atmospheric brightness temperature, $T_{b,atm}$, from the

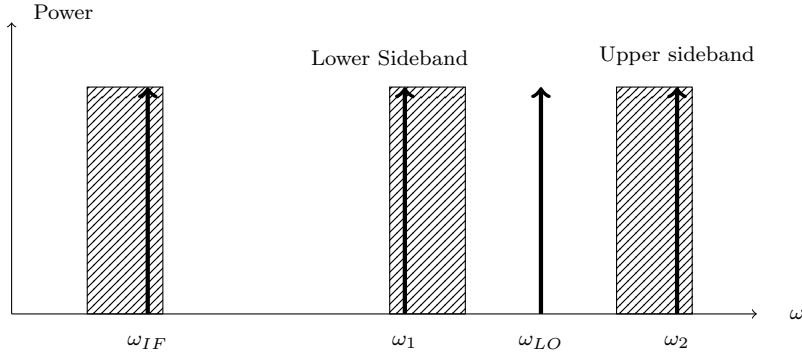


Figure 4.3: The heterodyne principle. When the RF signal is mixed with the LO signal (ω_{LO}), both frequency ω_1 and ω_2 will be mixed to the same intermediate frequency, ω_{IF} .

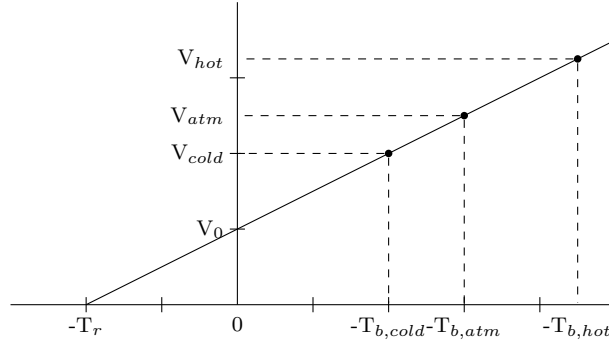


Figure 4.4: Calibration procedure in microwave radiometers. V_{hot} , V_{cold} and V_{atm} are the signals from the hot load, cold load and the atmosphere respectively. $T_{b,hot}$, $T_{b,cold}$ and $T_{b,atm}$ are the brightness temperatures from each measurement. V_0 and T_r are the receiver signal and temperature.

signal, V_{atm} , becomes

$$T_{b,atm} = \frac{T_{b,hot} - T_{b,cold}}{V_{hot} - V_{cold}} V_{atm}, \quad (4.1)$$

where subscripts *hot* and *cold* represent the signal and temperature of the hot and cold load, respectively. This calibration procedure is sufficient if the gain of the instrument is constant in time. However, most receiver systems will have time dependent variations in gain. In order to minimise the effect of these variations, a technique called Dicke-switching is used. Dicke-switching involves doing a differential measurement between a reference spectrum, $T_{b,ref}$, and the atmospheric spectrum, rather than measure the radiation from the atmosphere directly (Rohlfs and Wilson, 2008). The differential spectrum, ΔT_b , is then given by

$$\Delta T_b = T_{b,atm} - T_{b,ref} = \frac{T_{b,hot} - T_{b,cold}}{V_{hot} - V_{cold}} (V_{atm} - V_{ref}). \quad (4.2)$$

Since the errors from gain fluctuations are proportional to the total power measured, the receiver should be balanced. This means that the reference signal, V_{ref} , should

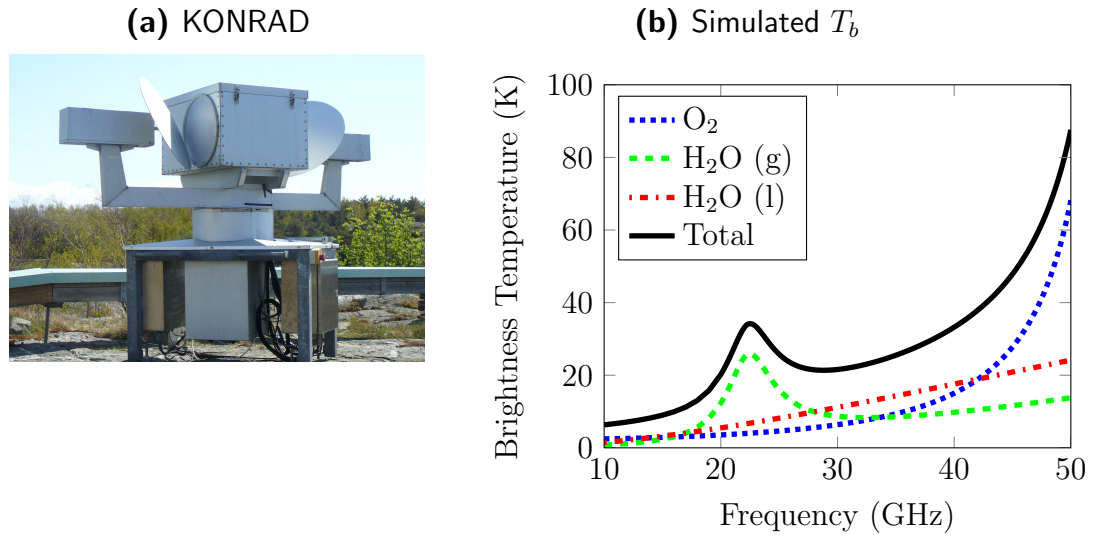


Figure 4.5: Left: A picture of KONRAD. Right: Simulated brightness temperature measured by an upward looking instrument (black), as well as the contribution from different species in the atmosphere. The atmosphere consists of 78 % N_2 , 21 % O_2 and has a water vapour column of 17 kg/m^2 and a liquid water column of 0.2 kg/m^2 .

ideally have the same power as the atmospheric signal V_{atm} .

4.3 Ground-based instruments

The aeronomy station at Onsala Space Observatory (OSO) has several ground-based radiometers with different purposes and operating at different frequencies. The two radiometers KONRAD and ASTRID are designed to retrieve tropospheric water content by measuring radiation on both sides of the 22 GHz water vapour line. Additionally OSO has a 22 GHz microwave radiometer designed for measuring mesospheric water vapour, and a 3 mm (113/115 GHz) radiometer which measures mesospheric carbon monoxide and ozone.

4.3.1 KONRAD and ASTRID

Figure 4.5a shows a picture of KONRAD, which together with its sister instrument ASTRID has two channels that measure radiation at 20.6/31.6 GHz and 21/31.4 GHz for the two instruments respectively. These channels are chosen so that they cover both sides of the water vapour line at 22.2 GHz. Figure 4.5b shows simulated brightness temperatures for a frequency interval relevant for these frequencies, including the contributions from molecular oxygen, water vapour and liquid water. Since the spectral behaviour of the absorption from liquid and gaseous water is different, is it

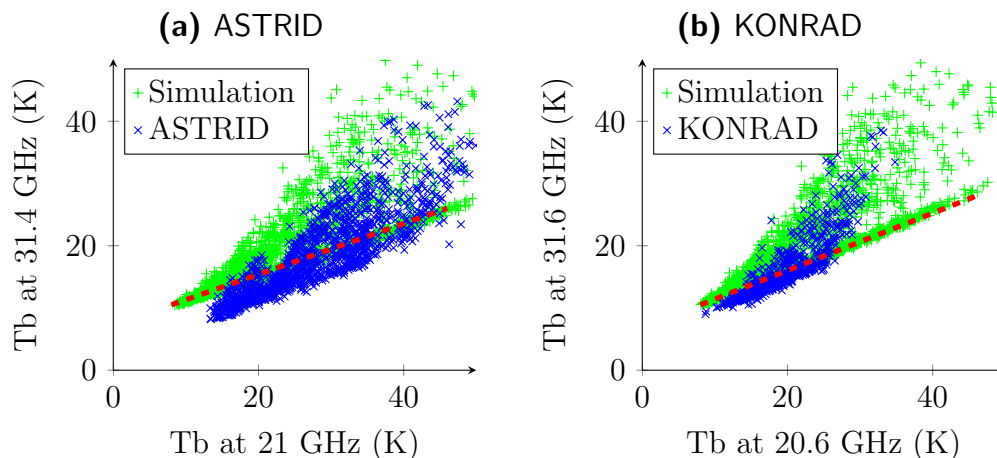


Figure 4.6: Simulated brightness temperatures (green, +) for the two channels on the ASTRID (a) and KONRAD (b) compared to measurements from the same instruments (blue, x). The simulated measurements along the dashed red lines are from atmosphere with a clear sky.

possible to separate the effect from the two of them when retrieving the tropospheric water content.

These instruments have traditionally been used to estimate the excess propagation path through the atmosphere for the light from distant stars due to water vapour. It is an important error source for geodetic very-long-baseline-interferometry measurements, where signals measured by radio telescopes at different points on Earth are combined to investigate the shape of the planet Earth. This excess propagation path, or delay, has been estimated by comparing a linear combination of the measured brightness temperature measured at the two frequencies, and the ground temperature with a regression model based on radiosonde measurements of the water content and a parameterisation of the ratio between liquid and gaseous water (Elgered, 1993). The retrieved path delays have been compared and found consistent with delays estimated by other methods at the OSO site (Ning et al., 2012).

Figure 4.6 shows the measured brightness temperature for KONRAD and ASTRID compared to brightness temperatures simulated in ARTS 2 using a set of atmospheres above the Onsala Space Observatory from the ERA-interim project as input (see Paper C). Each point measurement represents a 5 minute mean of measured the brightness temperatures from KONRAD/ASTRID. The figure shows a similar behaviour for both the simulated and measured brightness temperatures, with many measurements located along a line creating an abrupt lower threshold for the brightness temperature at 31.6/31.4 GHz for each measured brightness temperature at 20.6 GHz and 21 GHz. These points represent the “clear-sky” case, where no clouds are present, and are, for the simulated data, located along the dashed red line.

The seasonal variability of the atmosphere above OSO is seen in the variability

of the simulated data along the red line. The highest values are found during the summer and autumn when the troposphere is hot and wet, while the lowest values are winter and spring with a cold and dry troposphere. The measured KONRAD data shown only covers the period February to March, and hence the highest data points are not present in the right plot in figure 4.6.

When liquid water is present in the atmosphere, the 31.4/31.6 GHz channels measure higher brightness temperatures, resulting in data points far above the red line. Thus, from figure 4.6, the ability for these instruments to, at least qualitatively, differentiate between liquid and gaseous water is illustrated.

However, even though the structure of the brightness temperature across the two channels is consistent between the measurements and simulations, there is a clear offset between the two datasets. Assuming that for consistency we want the clear-sky line to overlap between the measurements and the simulations, an offset correction needs to be added to each of the instrument. This offset was estimated to $+3\text{ K}/+5\text{ K}$ for the 21 GHz and 31.4 GHz channels of ASTRID and $-2\text{ K}/1\text{ K}$ for the 20.6 GHz and 31.6 GHz channels of KONRAD.

Possible sources of this offset are many. First and foremost this could be related to the absorption models used for water vapour-, or oxygen in the simulations. However, since the difference between the two instruments is larger than any uncertainty in the forward model, we conclude that this error might as well be due to errors or uncertainties in the calibration or measurement procedure of the instrument. However, this requires further investigation before any clear conclusion can be drawn. We therefore decided to use KONRAD and ASTRID only as reference measurements in Paper C rather than using them directly in the tropospheric correction (see section 4.3.5).

4.3.2 The mesospheric water vapour radiometer at OSO

The 22 GHz microwave radiometer at OSO (figure 4.7a) measures water vapour in the mesosphere (Forkman et al., 2003a). Just like CO, water vapour is an excellent tracer of mesospheric dynamics due to its long photochemical lifetime in the mesosphere. Water vapour in the mesosphere is either water formed through the oxidation of methane, or water transported into the middle atmosphere through the tropical tropopause. This means that monitoring water vapour in the mesosphere can help us understand the influences of anthropogenic methane emissions on the mesosphere as well as provide information about the transport mechanics in the tropical tropopause.

Figure 4.7b shows a simulated atmospheric spectrum at the tropopause above OSO. The radio frequency coverage of the receiver is marked by the two black lines. The instrument has operated since 2001 and has provided over 10 years of data to the NDACC database.

During 2013 the instrument was fitted with a new backend, replacing the autocorrelator with a FFT spectrometer. This increased the bandwidth as well as the resolution of the instrument, allowing for retrievals over a larger range of altitudes. Data processing and validation of this new system is currently undergoing and we

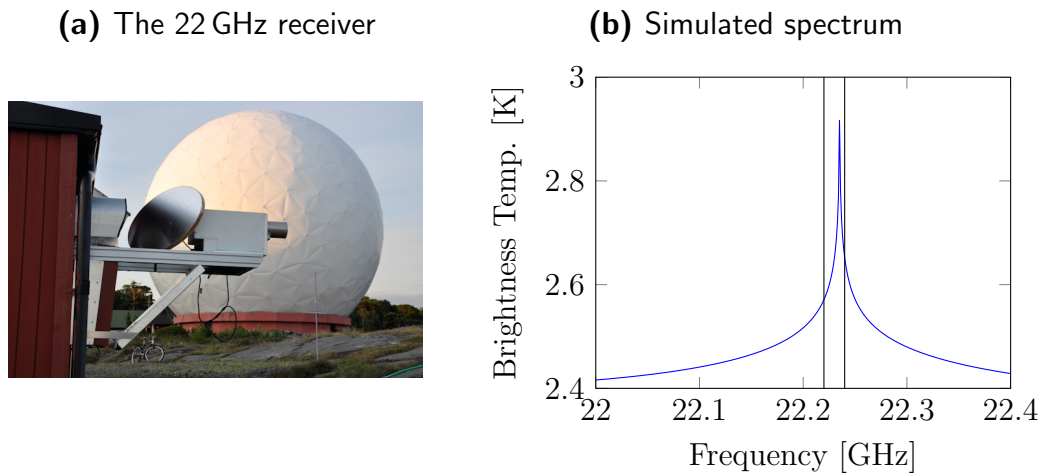


Figure 4.7: Left: A picture of the 22 GHz radiometer at OSO. Right: A simulated atmospheric spectrum of the frequencies around the 22 GHz water vapour line. The two black lines indicate the bandwidth of the 22 GHz instrument.

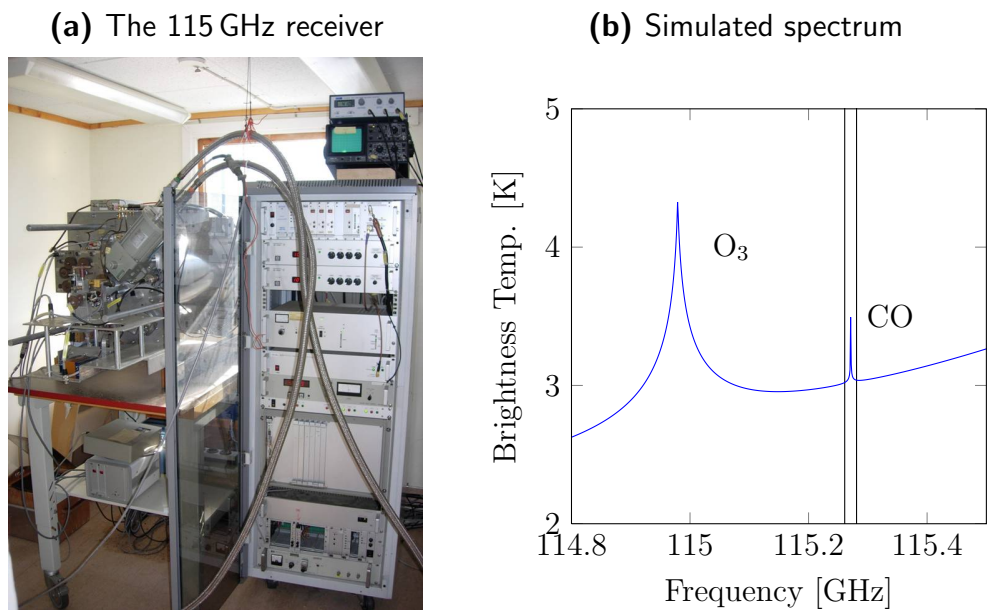


Figure 4.8: Panel a: A picture of the 115 GHz radiometer at OSO. Panel b: A simulated atmospheric spectrum of the frequencies around the 115 GHz CO line.

expect the first results to be available by fall 2015.

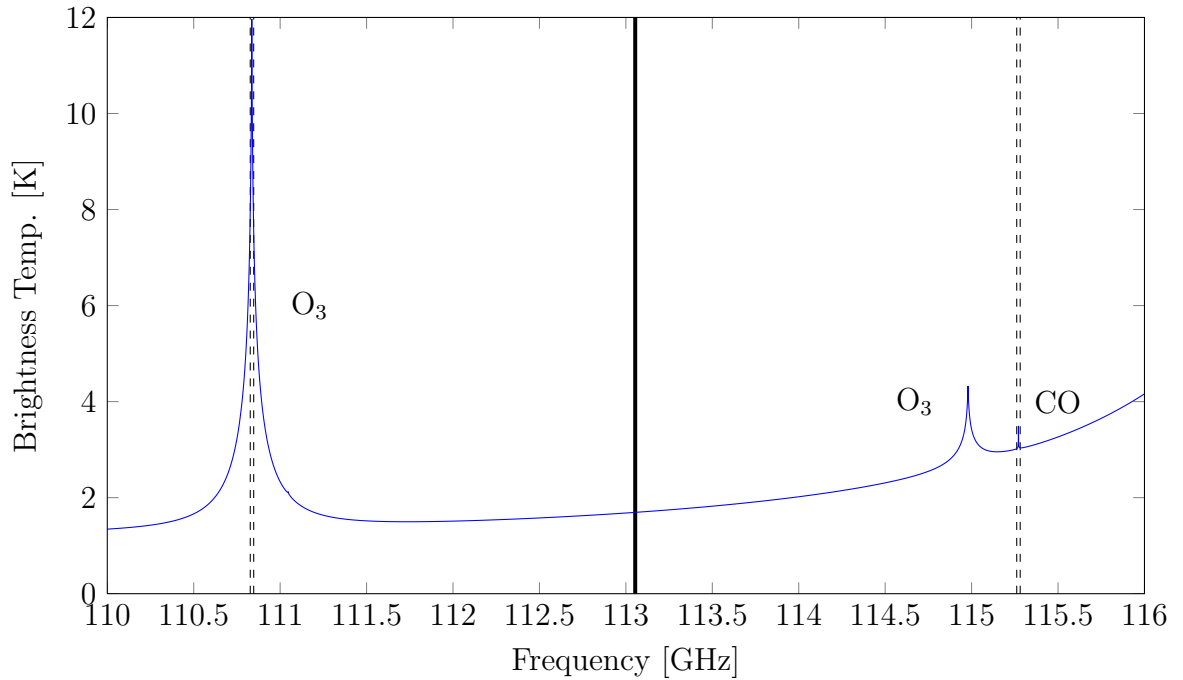


Figure 4.9: A simulated spectrum of the relevant frequencies for the new dual band instrument at OSO. The thick solid line shows the LO frequency. The dashed lines show the RF-coverage of the two bands.

4.3.3 The old CO radiometer at OSO

The 115 GHz microwave radiometer at OSO was designed to measure CO in the mesosphere (Forkman et al., 2003b). A picture of the instrument is shown in figure 4.8a. Figure 4.8b shows a simulated atmospheric spectrum as would be measured at the station without the influence of the troposphere. The troposphere is not included in the spectrum for pedagogical purposes as the tropospheric emission would obscure the CO line. The radio frequency coverage of the instrument is indicated by the two vertical black lines. The CO line at 115.27 GHz is situated on the wing of a wide O_2 line located at 118 GHz, close to an O_3 line at 115 GHz. The 115 GHz radiometer at OSO was operated from 2002 to 2008 when it was disassembled for a major overhaul. This six year time series from the OSO radiometer is still the longest continuous ground-based observation of CO in the mesosphere.

4.3.4 The new CO/ O_3 radiometer

As mentioned in section 4.3.3, the 115 GHz radiometer was taken down for a major overhaul in 2008. During this overhaul several changes to the instrument were made, and the new instrument will be referred to as the 113 GHz radiometer in this thesis. One of the changes made was to move the LO frequency to 113.054 GHz and

remove the sideband filter. This allows for simultaneous observations of O₃ and CO (see figure 4.9). One limitation is however that the ratio between the gain in the two sidebands needs to be known within at least $\pm 5\%$ not to have to large of an influence on the final result. To measure this is not trivial, as finding stable RF sources and ensuring that the connection and disconnection of these do not contaminate the measurements requires a accurate understanding of the frequency behaviour of not only the instrument, but the system used to characterise it as well. The instrument, measurement of the sideband ratios as well as the first results from this instrument is described in detail in Paper C.

4.3.5 Tropospheric correction

Single Layer troposphere

Ground-based microwave radiometers designed to measure the mesosphere need to account for the attenuation of the mesospheric signal as it passes through the troposphere. One way to account for this, is to solve the radiative transfer equation (equation 3.8) for a single layer troposphere with an effective temperature T_{eff} , and a tropopause at z_{trop} . The solution is given by

$$T_{b,atm}(z_g) = T_{b,atm}(z_{trop})e^{-\tau_{trop}} + T_{eff}(1 - e^{-\tau_{trop}}), \quad (4.3)$$

where τ_{trop} is the optical thickness of the troposphere along the measured propagation path and z_g the altitude of the instrument. To solve this equation for $T_{b,atm}(z_{trop})$, τ_{trop} and T_{eff} , must be determined. The optical thickness can be estimated using e.g. a tipping curve measurement, where the opacity is determined by measuring the tropospheric radiance at different angles (e.g. Straub et al. (2010)). Another option is to apply an empirical model of the troposphere. Using direct measurements of the atmosphere such as radiosondes, or simulated measurements, a regression model can be fitted to establish the relationship between T_{eff} and input variables such as $T_{b,atm}(z_g)$, surface temperature, surface pressure, or any other measured variable (e.g. Forkman et al. (2003a)). Once T_{eff} is estimated, the optical thickness, τ_{trop} , can be estimated from

$$e^{-\tau_{trop}} = \frac{T_{eff} - T_{b,wings}(z_g)}{T_{eff} - T_{b,wings}(z_{trop})}, \quad (4.4)$$

where $T_{b,wings}$ is measured brightness temperature at the line wings and $T_{b,wings}(z_{trop})$ the brightness temperature at the wings above the troposphere. For the ground-based radiometers at OSO $T_{b,wings}(z_{trop})$ is assumed to be equal to the cosmic background radiation.

Direct Modelling / Retrieving the troposphere

If tropospheric attenuation varies greatly across the bandwidth of the instrument, the single layer tropospheric correction cannot be used. Another option to correct for the tropospheric influence is by estimating the atmospheric state above the radiometer,

Channels	21 GHz	31.4 GHz	113 GHz
Measured T_b	31.00 K	25.46 K	133.88 K
ASTRID	0.19 K	-0.87 K	5.93 K
ASTRID + 113 GHz	-1.23 K	-0.52 K	1.94 K
Retrieval	-0.38 K	-1.1 K	0.88 K

Table 4.1: The measured brightness temperatures from ASTRID and the 113 GHz radiometer for an example measurement at OSO recorded 31. October 2014 (second row). The three following rows are the residuals ($T_b^{fitted} - T_b^{measured}$) of fits using three different methods: Fitting the two channels of ASTRID (ASTRID), fitting ASTRID and the 113 GHz radiometer (ASTRID + 113 GHz), and including the troposphere and the instruments in directly in the state and measurement vector of the mesospheric retrieval (Retrieval).

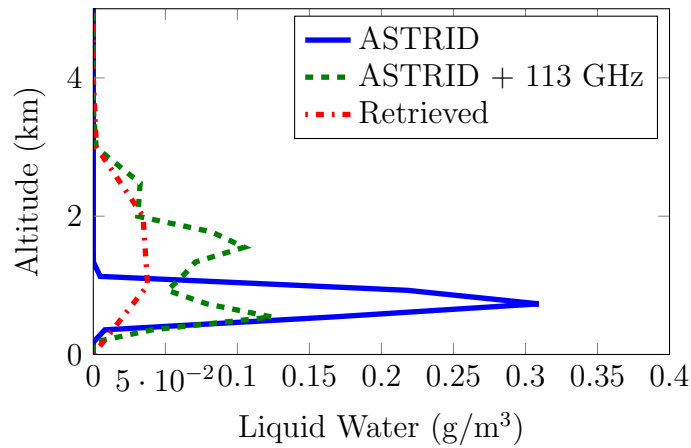


Figure 4.10: The amount of liquid water in the troposphere fitted using the three different tropospheric correction methods for the same measurement as in table 4.1.

either by using a model (e.g. weather prediction) or auxiliary measurements (e.g. radiosondes), and then including this troposphere directly in the forward model.

During the work on retrieving data from the 113 GHz receiver, three different methods for estimating the troposphere were tested. The first compared the brightness temperature measured at the two channels one of the tropospheric radiometers (KONRAD or ASTRID) with a set of forward model calculations where the tropospheric temperature, water vapour and liquid water profiles were extracted at the OSO site from the ERA-interim project (Dee et al., 2011). The tropospheric scenario where the simulated brightness temperatures had the best fit to the measured brightness temperatures was then selected and used as the troposphere for the mesospheric retrievals. Furthermore, a second method was tested where the mean brightness temperature across all channels of the the 113 GHz receiver was also simulated and included in the fitting procedure. Finally, since the ERA-interim scenarios do not cover all the possible tropospheres above Onsala, a further adjustment was made

by including the troposphere in the state vector and the measurements from KONRAD/ASTRID into the measurement vector. The troposphere could then be retrieved together with the mesospheric data using the MAP method described in section 3.4.

Table 4.1 shows the results of a tropospheric correction from an example measurement at OSO. Ideally the simulated brightness temperatures should exactly match the measured values (no residuals). The method of including the troposphere in the state vector (Retrieval) resulted in the best combined fit considering all the three frequencies, whereas the two methods where no retrieval was performed (Radiometer, Radiometer + 113 GHz) have problems fitting all three frequencies.

As discussed in section 3.4 simply retrieving an atmospheric profile which fits a set of measurements might lead to unrealistic or unphysical results. Thus, inspecting the retrieved quantities and ensuring that the modelled troposphere is realistic is important. Figure 4.10 shows the tropospheric liquid water profile resulting from the three different methods in table 4.1. The retrieved profile has less structure than the profiles selected from the ERA-interim scenarios, due to the fact that there are not enough independent pieces of information in the measurements to resolve vertical structures. But apart from this structure, the retrieved profile is certainly reasonable, and thus including the tropospheric water vapour radiometers (ASTRID / KONRAD) in to the mesospheric retrievals has the possibility to provide an accurate tropospheric correction method. However, due to the discrepancies seen in the two tropospheric instruments (see section 4.3.1) these instruments were in the end not used, and in Paper C the troposphere was retrieved using only the mean brightness temperature across the 113 GHz radiometer. This does, however, reduce the precision of the retrieved mesospheric profiles somewhat (up to 0.5 ppmv for CO at the highest altitudes).

4.4 Satellite instruments

While ground-based instruments are excellent for measuring the atmosphere over a single area on Earth, a satellite-based instrument is advantageous if global coverage is wanted. Measurements from satellites can be performed using several different geometries. Figure 4.11 shows examples of different viewing geometries and methods for satellite-based instruments. In particular there is a distinction between downward looking instruments, and limb sounding instruments which looks along the tangent of the Earth. Downward looking instruments have (in general) good horizontal resolution, while limb sounding is beneficial when the vertical structure of the atmosphere is sought after. The altitude at which the line-of-sight of a limb sounding instrument is parallel to the surface of the Earth is called the tangent altitude.

In general a distinction is also made between active instruments, where a synthetic signal is sent through the atmosphere to acquire the desired information, and passive measurements that rely on natural sources of radiation. These natural sources can be thermal radiation from the atmosphere or solar radiation, either by directly observing the atmospheric absorption of sunlight (solar occultation) or using the sunlight

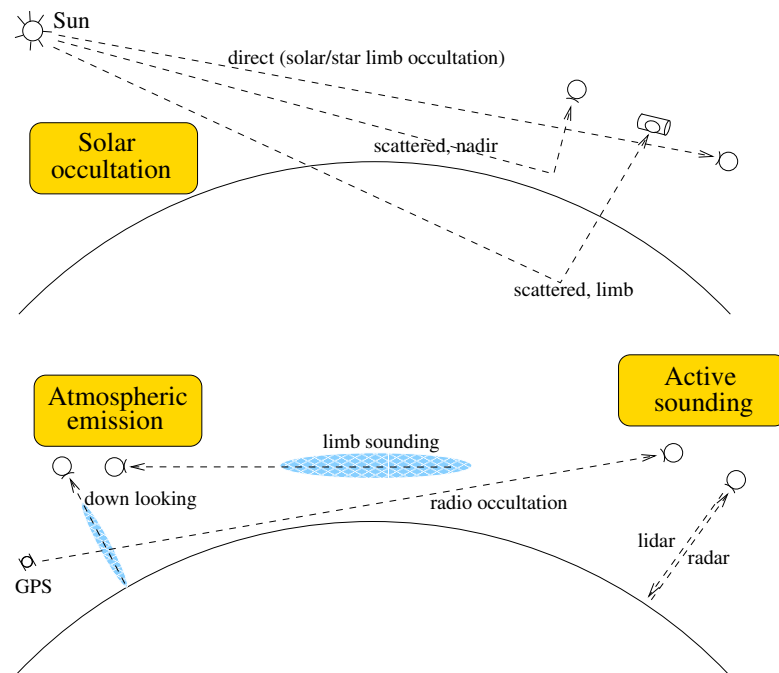


Figure 4.11: Overview of different measurements geometries for satellite instruments (figure courtesy of Patrick Eriksson).

scattered by the atmosphere (limb scattering).

Each method has its own advantages and disadvantages. Methods using atmospheric emission are naturally not reliant on solar light, and can thus measure the atmosphere during nighttime as well, whereas methods relying on solar illumination can offer a stronger signal. Additionally, the choice of method will depend on which transitions and what wavelengths to use.

To achieve global coverage, Earth-observing satellites are often placed in polar orbits. This means that the satellite orbits the Earth close to perpendicular to the equatorial plane, and by allowing the Earth to rotate under the satellite it can provide a global map of the measured quantities. A particular type of polar orbit is the, sun-synchronous orbit. Here the orbital inclination (the angle between the orbital plane and equator) is selected such that the satellite crosses any particular latitude at the same local time for each orbit. To achieve this, the orbit is designed such that the precession of the orbit due to the asphericity of the Earth exactly matches the average angular speed at which the Earth orbits the sun (Rees, 2001). This puts strong limitations on the selection of orbital parameters, such that for a satellite at e.g. 800 km the orbit inclination must be 99° , i.e. retrograde.

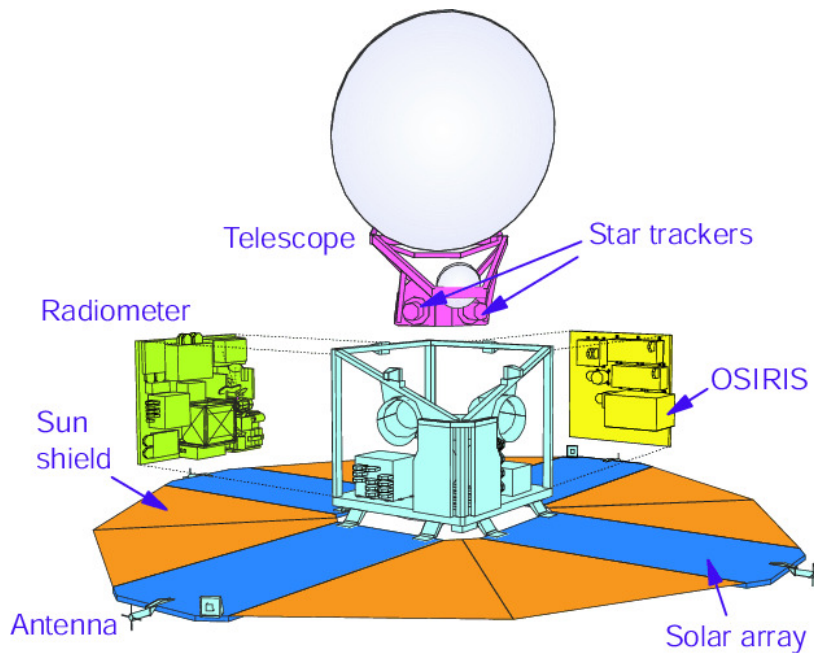


Figure 4.12: Overview of the Odin satellite (Nordh et al., 2003).

4.4.1 Odin

Odin is a Swedish led international satellite project launched on 20 February 2001 (Murtagh et al., 2002). It flies in a sun-synchronous polar orbit at ≈ 600 km with an equator crossing time of 18.00 (ascending). It has two instrument on board, the Sub-Millimetre-Radiometer (SMR) and the Optical Spectrograph and Infra-Red Imager System (OSIRIS). At the start of the satellites lifespan it had two missions, with observation time split between the astronomy and aeronomy. Since 2007 however, the satellite has been wholly dedicated to atmospheric observations. Figure 4.12 shows the layout of the Odin satellite, with the SMR (radiometer) and OSIRIS on each side of the satellite and the 1.1 antenna clearly seen at the top of the figure.

SMR

The radiometer, SMR, was designed to measure water vapour and carbon monoxide in outer space, as well as on Earth. Additionally, species important for ozone chemistry (ozone, ClO, NO_x , and others) were of interest for the atmospheric mission whose goals are described in Murtagh et al. (2002). These considerations resulted in an instrument consisting of 4 channels in the sub-millimetre region, covering frequencies from 486-581 GHz, and one in the millimetre wavelength region measuring the spectral line of molecular oxygen at 118 GHz.

An overview of the SMR instrument is shown in figure 4.13. The instrument has two blocks of receivers, A and B/C. These blocks are further divided into sub-blocks A1/A2, B1/B2 and C, each with their own local oscillators and mixers. The

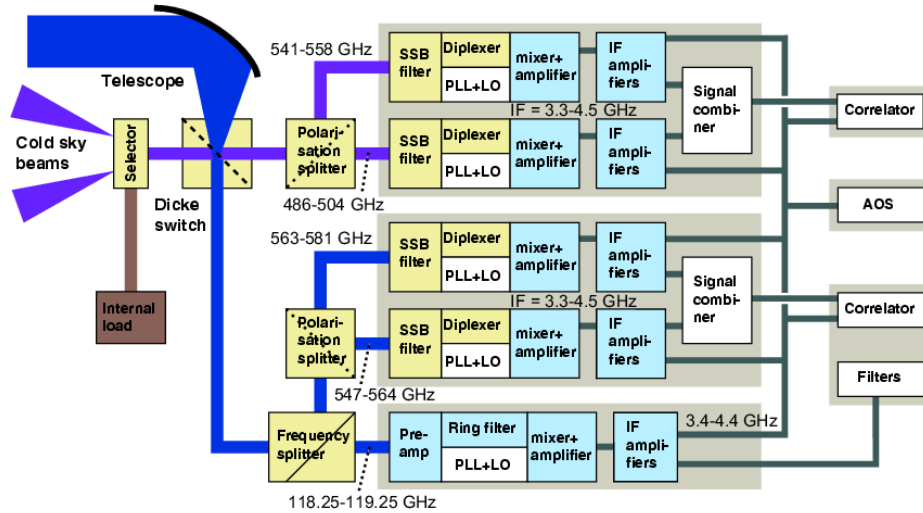


Figure 4.13: Overview of of the sub-millimetre radiometer (SMR) on board Odin (Frisk et al., 2003).

backends consist of four different spectrometers, two hybrid autocorrelators (AC1 and AC2) with adjustable bandwidths between 100 MHz to 800 MHz, an acousto-optical spectrometer with a 1 GHz bandwidth, and a 3-unit filterbank spectrometer dedicated to measure the 118 GHz O_2 line. This combination of front and backends makes SMR a very flexible instrument, with the possibility to measure a myriad of spectral lines over a wide range of frequencies. In this thesis, data from SMR has been used both for validating the ground-based carbon-monoxide measurement at OSO and retrieving water vapour and temperature in the polar summer mesopause region.

For the measurement of CO the B1 frontend is used in combination with the AC1 correlator. It measures the $J=5 \rightarrow 4$ (576.27 GHz) rotational transition of CO. For these measurements the satellite scans altitudes from 20-105 km. The retrieval precision is around 20% (Dupuy et al., 2004). The major issue with the Odin measurements has been a problem with the local oscillator used, resulting in many corrupt spectra. This, combined with the fact that the Odin aeronomy mission shared observation time with the Odin astronomy mission during the intercomparison period, means that relatively few CO measurements were available for intercomparison with the OSO radiometer.

For the measurement of water vapour, the strong spectral line at 556.9 GHz is used. This can be measured using two different frontends. Both the A1 and B2 frontend were designed to measure this line to provide redundancy in case of problems with the instrument (as for example with the B1 frontend). Both settings use the AC1 autocorrelator, and the two modes are referred to as frequency mode 19 and 13 respectively. However, studying the spectra revealed a systematic offset in brightness temperature between the two modes. To investigate this, both modes were run simultaneously (using two different autocorrelators, AC1 and AC2) for a few orbits during 2014. Figure 4.14 shows a mean of several spectra at different tangent altitudes by

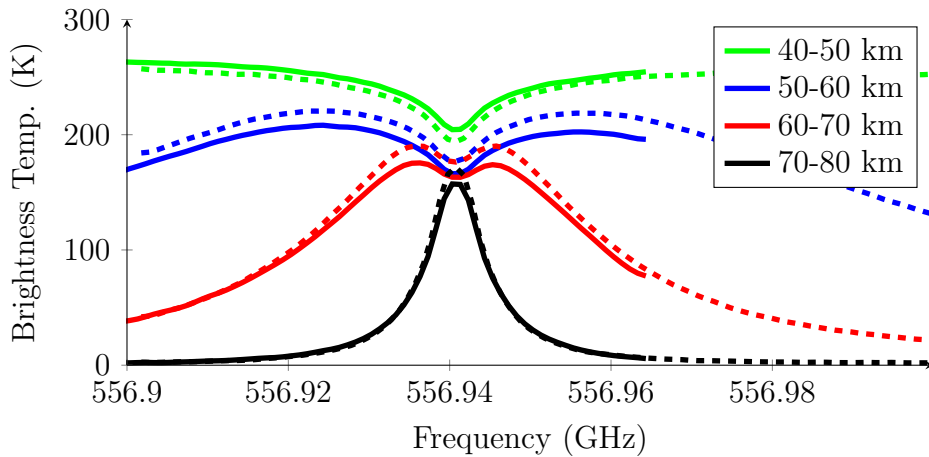


Figure 4.14: Mean of spectra of the 557 GHz water vapour line recorded by Odin-SMR using the A1 (solid) and B2 (dashed) frontends during an orbit. Each curve corresponds to the mean of all spectra with tangent heights between the labelled altitudes.

mode 13 and 19 respectively during these test orbits. A clear offset between the modes can be seen, and as the spectra from the two modes are recorded within 1 second of each other, this offset is clearly not physical. The exact reason for this off-set is not known, but is most likely linked to bad performance of the sideband filter of frontend A1. In Paper D we compare retrievals using each of the modes to other instruments, and conclude that the best agreement between SMR and the other instruments is achieved using frequency mode 13. This is actually contradictory to previous studies where frequency mode 19 is considered the most reliable (e.g. Lossow et al. (2009)). However, since the measurements used in Paper D only look at a small region of the atmosphere and some details in the measurement procedure differs from the standard measurements, our conclusions may not be applicable to the standard measurements.

OSIRIS

The second instrument on board Odin, OSIRIS, has two sub-systems (Llewellyn et al., 2004). One is an infrared imager, which collects atmospheric airglow from the vibrational-rotational states of O_2 and OH near 1270 nm and 1530 nm. The atmospheric temperature can be retrieved from these emission lines since the occupational distribution of the rotational states is highly dependent on the ambient temperature. The second sub system is an optical spectrograph operating at wavelengths between 280 to 800 nm. The spectrograph uses scattered sunlight as a source (see figure 4.11). By comparing the absorption spectra from these measurements to simulated spectra (also called Differential Optical Absorption Spectroscopy), the concentration of species such as ozone and NO_2 at different altitudes can be estimated.

For the studies in this thesis, OSIRIS is used to measure ice particles in the mesopause region. This can be done since the scattering of UV light increases in the

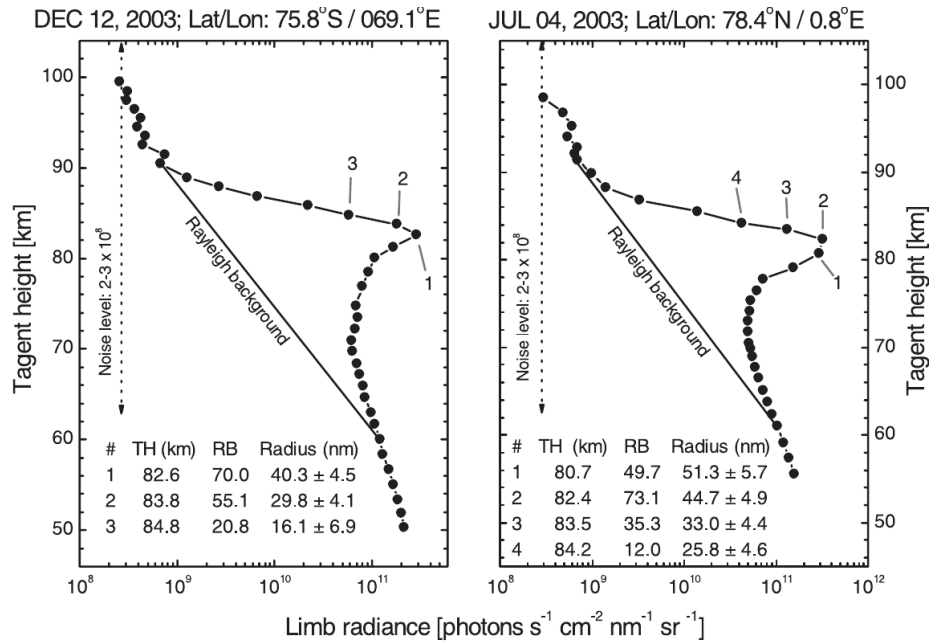


Figure 4.15: Radiance measurements of PMCs from OSIRIS. Notice the increase of radiance compared to the Rayleigh background (von Savigny et al., 2005).

presence of these particles, in the same way that normal clouds increase scattering in the troposphere thus giving them their distinct white colour. Figure 4.15 shows the radiance at a wavelength of 300 nm from some example measurements, clearly showing the increase in brightness from PMCs around 80 km.

The PMC measurements by OSIRIS have previously been used in many studies to investigate PMCs (e.g. Feofilov and Petelina (2010) and Gumbel and Karlsson (2011)). However, one noticeable feature of figure 4.15 is the fact that the increased brightness from the clouds are seen all the way down to 60 km. The reason for this is that clouds close to the satellite (compared to the tangent point) will appear at lower altitudes than their true altitude. To mitigate this issue, as well as improve the horizontal resolution a special set of measurements were performed during the polar summers of 2010-2015 where OSIRIS (and SMR) was operated in a special tomographic mode (Hultgren et al., 2013). By scanning a limited altitude range overlapping measurements can be achieved (see figure 3.8) and a tomographic retrieval can be performed.

The method used in the OSIRIS retrievals is the so called Multiplicative Algebraic Reconstruction Technique (MART) (Lloyd and Llewellyn, 1989; Degenstein et al., 2003). Similarly to the MAP method discussed in chapter 3.4 it returns the most likely atmosphere given the measured data. However, unlike the MAP method, it is a maximum likelihood method, meaning that it uses no a priori information in its estimation, hence it is an unconstrained method. Furthermore, the MART technique assumes that the measurement noise follows a Poisson distribution.

MART applies an iterative technique to estimate the true atmosphere. Using the

nomenclature from section 3.4, the estimation of the j^{th} element of the state vector at the n^{th} iteration is given by

$$\hat{x}_j^{(n)} = \hat{x}_j^{(n-1)} \sum_i \left(\frac{y_i}{\hat{y}_i^{(n-1)}} \beta_{ij} \right), \quad (4.5)$$

where \sum_i indicates summing over the elements of the measurement vector and $\hat{y}_i^{(n-1)}$ is the i^{th} element of the estimated measurement vector given by

$$\hat{\mathbf{y}}^{(n-1)} = \mathbf{K}\hat{\mathbf{x}}^{(n-1)}. \quad (4.6)$$

In the work used in this thesis, the quantity retrieved from OSIRIS is the brightness of the scattered light at each grid point. Thus the weighting function (assuming low opacities) is simply the distance covered by the line-of-sight of the measurement through the grid box represented by the retrieval grid point. Finally, β in equation 4.5 is a weighting term (not to be confused with the weighting function) which in the case of brightness retrieval is equal to the distance of a single line-of-sight going through a retrieval gridbox divided by the total distance covered by all measurements through that grid box:

$$\beta_{ij} = \frac{K_{ij}}{\sum_i K_{ij}}. \quad (4.7)$$

To execute MART, an initial state vector $\hat{\mathbf{x}}^0$ is selected and equation 4.5 is iterated until convergence is reached (i.e. changes between iterations are sufficiently small). It should be noted that even though the MART algorithm contains no explicit regularisation, in the case where multiple solutions of equation 3.11 exists, the solution chosen by the MART method will depend on the selection of $\hat{\mathbf{x}}^0$ (Shepp and Vardi, 1982).

By comparing the retrieved brightness from the clouds at different wavelengths information can be extracted about the size, and hence the number and total mass of the ice particles at a grid point. The reason for this is that the wavelength dependency of the amount of light scattered by a particle depends on its size. For particles much smaller than the wavelength (Rayleigh regime) the amount of scattered light is proportional to λ^{-4} whereas for much larger particles the scattering is essentially independent of wavelength. An estimate of the particle size can therefore be found by calculating the λ exponent (called Ångström exponent) from the measurements. Figure 4.16 shows the calculated Ångström exponent for an ensemble of particles. As long as the particles have a mode radius smaller than 100 nm, the Ångström exponent drops monotonously, but passing 100 nm it starts increasing again, meaning that there is not a unique mode radius fitting to a measurement. However, measurements at other wavelengths indicate that areas with mode radius larger than 100 nm are unlikely and thus a reasonable assumption is that the smallest radius should be used in the case of multiple solutions. Once the mode radius is found, the number density and mass density of the cloud can be calculated. It should be noted that all

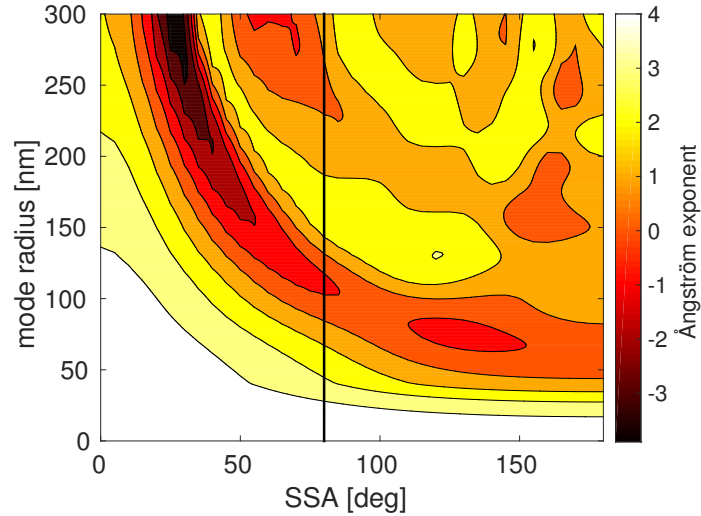


Figure 4.16: The calculated Ångström exponent for UV wavelengths at different scattering angles (SSA) for an ensemble of oblate spheroid ice particles (axial ratio = 2) adhering to a Gaussian particle size distribution (Baumgarten et al., 2010). The black line indicate the approximate scattering angle of the OSIRIS instrument. Data courtesy of Susanne Benze.

these parameters (radius, number density and mass density) depend highly on the assumptions of the particle size distribution (Hultgren and Gumbel, 2014).

4.4.2 Other Satellite instruments

In the studies conducted in the framework of this thesis, data from a number of other satellite instruments were used to cross compare and validate our own measurements. These include ACE-FTS, Aura-MLS, ENVISAT-MIPAS and AIM-SOFIE, and the satellites carrying the instruments are shown in figure 4.17. The instruments operate at different wavelengths and use different methods for measuring the atmosphere.

The Canadian Atmospheric Chemistry Experiment (ACE) on board SCISAT was launched on 12 August, 2003 (Bernath et al., 2005). It has a 74° inclined circular orbit at 650 km. The primary instrument on board is the high resolution Fourier transform spectrometer (ACE-FTS) which makes infrared absorption measurements of the atmosphere along the limb using the sun as a source (see figure 4.11). ACE-FTS measures over a large range of altitudes covering 5-105 km under clear-sky conditions. In Paper A and Paper D we use the carbon monoxide, water vapour and temperature data from ACE to validate our own results.

The Solar Occultation For Ice Experiment (SOFIE) is, similarly to ACE-FTS, a solar occulting instrument measuring the absorption of solar light by molecules and aerosols in the atmosphere. It flies on the AIM satellite which launched 25 April, 2007. The AIM mission was specifically designed to measure the properties of, and the atmosphere around polar mesospheric clouds. This instrument is used in Paper

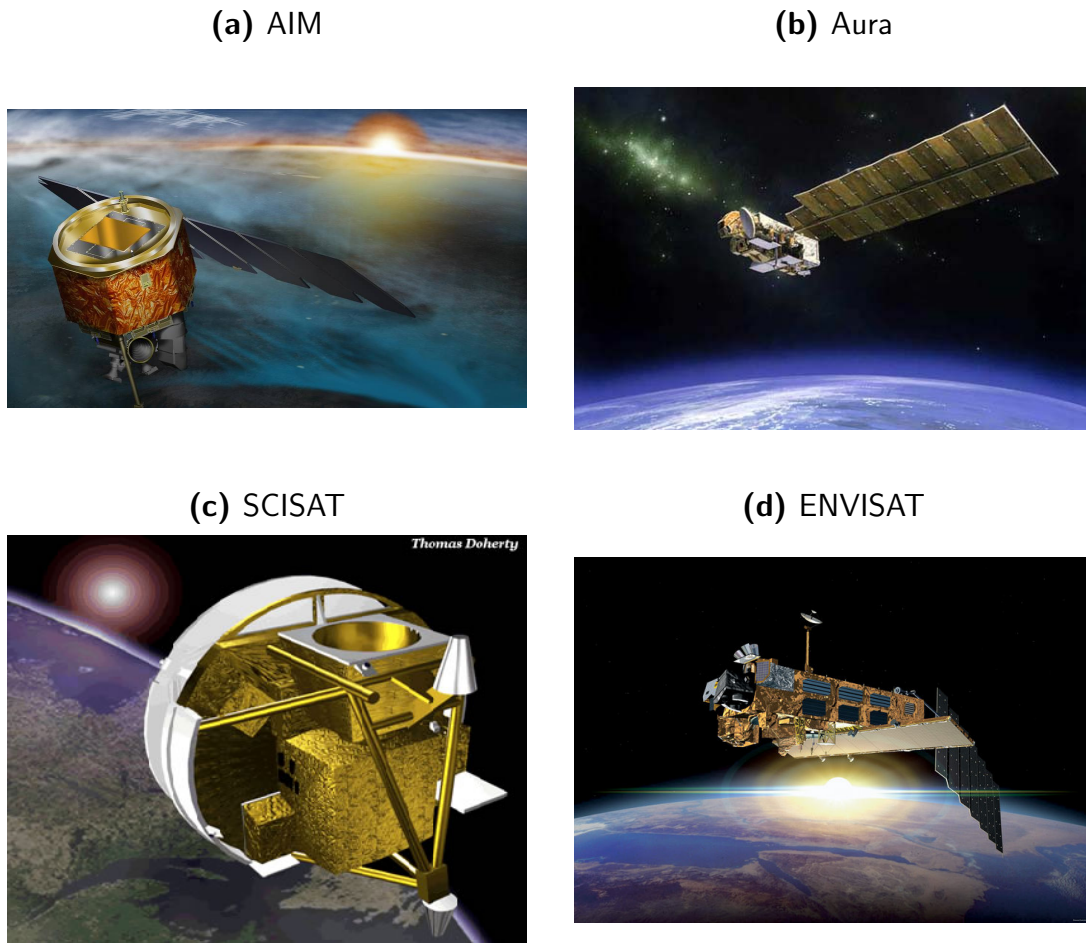


Figure 4.17: Some of the satellites used in this thesis. Images from CSA, ESA and NASA.

D as the main source of comparison of our retrieved water vapour and temperature data around PMCs.

Using the sun as a source for absorption measurements allows for a strong signal, but solar occultation instruments are limited to performing measurements twice per orbit (sunrise and sunset). Emission sounders (such as SMR) do not have this limitation, and we use two different emission limb sounding instruments (in addition to SMR) in Paper A to provide additional data sources for the carbon monoxide comparison.

The Microwave Limb Sounder (MLS) is located on the Aura satellite that was launched by NASA on 15 July 2004 (Schoeberl et al., 2006). It flies in a sun-synchronous near-circular polar orbit at an altitude of 705 km with an equator crossing time of 13.45 (ascending node). It retrieves CO concentrations between 15-85 km, with a vertical resolution of 4-8 km in the mesosphere. The precision of a single retrieved profile is very poor, exceeding 100% above 20 km. The basic reason for this

poor precision is the low signal-to-noise ratio in the measurements (Pumphrey et al., 2007). MLS does however provide numerous measurements, and by averaging these, the data become useful.

The Michelson Interferometer for Passive Atmospheric Sounding (MIPAS) on board ENVISAT, also measures atmospheric emission from the CO molecule, but in the infrared wavelength region. ENVISAT is a research satellite launched in March 2002 (Louet and Bruzzi, 1999) which flies in a sun-synchronous polar orbit with a 10.00 equator crossing time (ascending node). MIPAS has a much higher precision than MLS but in the upper atmosphere the infrared emission lines are highly affected by non-LTE processes, thus requiring a more complicated forward model and retrieval scheme (e.g Fischer et al. (2008)).

In summary, the instruments used in this thesis all have their own advantages and disadvantages. In the validation papers of this thesis we have tried to use the instruments which provide the most relevant and comparable results to validate our own data. The number of instruments used, and the thoroughness of the validation depends on the scope of the paper and size of the dataset. Paper A used four external instruments, Paper D used two and Paper C used only a single external instrument for the comparison of data.

Summary of Papers

5.1 Summary Paper A

The large scale dynamics of the mesosphere can be studied by the use of tracer species. These are species that have a long photochemical lifetime, and by looking at the distribution of these species compared to their sources, we can determine how they are advected by the general circulation. One such tracer species is carbon monoxide, CO. At the aeronomy station at the Onsala Space Observatory, CO has been measured from a ground-based microwave spectrometer from 2002-2008. Simultaneously several satellites have been measuring the global distribution of CO. By cross comparing the measurements we estimate the systematic errors of the spectrometer, and give indications of possible discrepancies between the satellite datasets.

Paper A uses four satellites to evaluate the performance of the instrument located at OSO, so that the uniquely long measurement series it provides can be better used for atmospheric studies. The paper concludes that the systematic error in the measurements is less than 20 % between 2004-2008. During this period the OSO measurements are consistent with the satellite instruments. However, the measurements show up to 25 % higher CO column values above 70 km compared to the satellite instruments. This is within the combined error margins of the instruments, but indicate a possible bias in either the ground-based or satellite measurements. In the period between 2002-2004 the consistency between the different measurements is less clear. The differences between the different satellite instruments are ± 50 %, and the measured CO concentration from OSO is located somewhere in between.

My main work in this study was to set up and perform the retrievals for this instrument in close collaboration with Patrick Eriksson. The instrument itself is built and operated by Peter Forkman. The satellite comparison was initiated when we started comparing the CO data to atmospheric models and realised that we lacked a proper error quantification for the data set. With the help of Jo Urban, I downloaded satellite data, performed the collocations, interpreted the results and presented them

in the paper.

5.2 Summary Paper B

An old meteorologist joke is that “when in doubt go for persistence”, meaning that a good predictor of tomorrow’s weather is that it will be the same as today. In Paper B we present a retrieval algorithm for ground-based radiometers that take into account this temporal correlation in atmospheric states. Retrievals for ground-based instruments are usually performed on each measured spectrum individually. Our paper, “Time series inversion of spectra from ground-based spectrometers”, takes a multi-dimensional approach. Using several spectra, we retrieve an entire time series simultaneously. This is the first time such an approach has been used for a ground-based microwave spectrometer.

The method offers several advantages over traditional single spectrum retrievals. First and foremost it allows for variable temporal resolution at different altitudes. This means that the optimal compromise between signal to noise ratio and temporal resolution can be made at each altitude separately rather than choosing an ad-hoc integration time before performing the retrievals. Other advantages include the possibility of seamlessly interpolating and re-gridding data in the temporal domain during the retrieval. These findings should help improve retrievals for future radiometers observing the middle atmosphere.

This study is based on an idea by Patrick Eriksson. I implemented and evaluated the method and wrote up the paper presenting it. This included exploring the effects of different a priori correlation functions and comparing it to traditional averaging methods, as well as applying the method on the 22 GHz water vapour radiometer at OSO.

5.3 Summary Paper C

To keep costs down and increase the scientific value of ground-based microwave radiometers it is important to utilise each instrument to its fullest. One way of doing this is to simultaneously measure several species. During 2009-2010 the CO instrument described in Paper A underwent a major upgrade. By removing the sideband filter, and changing the LO-frequency to 113.054 GHz the instrument was converted to operating in a dual sideband mode. By doing this, the instrument now has the ability to measure both the CO line at 115 GHz and ozone 111 GHz simultaneously. This is the first time such capabilities have been shown in a ground-based microwave radiometer, and Paper C describes the instrument and the first results after it resumed operations in the autumn of 2014.

Comparing the results to Aura-MLS we find a good agreement between the values observed by the ground-based instrument and MLS. Similar to the conclusions drawn in Paper A the ground-based instrument seem to overestimate the concentrations at

high altitudes compared to MLS, though we cannot say whether this is due to intrinsic differences in the methods used, or inaccuracies for each individual instrument.

Peter Forkman and I planned and structured the paper together, and my main contribution was to set up and present the retrievals as well as investigating possible methods to perform tropospheric corrections for the instrument. The work included using and interpreting data from the two total power radiometers at OSO, exploring possible errors from the sideband characterisation and interpreting the final data product.

5.4 Summary Paper D

To understand the formation of polar mesospheric clouds, and to predict what will happen with them in the future we need to know how the background atmosphere influence these clouds. In particular the ambient temperature and the amount of available water are known to be critical for cloud existence. To this date few measurements have been performed where both the clouds and these two variables have been simultaneously measured, and no measurement has yet been able to sample horizontal as well as vertical structures of both the clouds and their background atmosphere.

In paper D we utilise SMR to perform a set of special measurements to retrieve water vapour and temperature in the summer mesopause region with an horizontal and vertical resolution better than $300 \text{ km} \times 2 \text{ km}$. To achieve this high resolution the measurements were done in a tomographic fashion measuring the same geographic location from several different angles. Applying a two-dimensional retrieval approach the atmospheric field along the orbit path could be reconstructed. This was the first time ARTS has been used for tomographic retrievals. The results were compared to ACE-FTS and AIM-SOFIE, and found to be in general agreement with regards to one of the two operating modes of SMR.

Paper D presents what probably is the main result of this thesis, the work involved collaboration with colleagues both on the instrument and retrieval side as well as establishing cooperation with my co-authors from Stockholm University. Most of the work in setting up the retrievals, performing the error analysis and comparing the data with other instruments was done by me, as well as writing up the paper, planning and presenting the study.

5.5 Summary Paper E

The tomographic dataset from the Odin satellite provides a unique opportunity to study the relationship between the background atmosphere and the polar mesospheric clouds. Paper E uses the tomographic data from SMR to calculate the amount of ice expected in the atmosphere assuming thermodynamic equilibrium, and compares this to simultaneous measurements of cloud parameters, mainly ice mass density, per-

formed by OSIRIS. In agreement with previous studies we find that OSIRIS measures less ice than predicted by assuming equilibrium. However, the equilibrium model can reproduce several of the general features observed such as the variation in altitude, latitude and across the season.

During this study we also found clouds existing far below the region of supersaturation. Due to the short time it would take for these observed cloud pixels to sublimate, and the fact that they are seen up to several km below the region of supersaturation, we conclude that these low altitude cloud regions cannot be explained by sedimentation alone, as has been suggested in previous studies.

Finally, using a simple growth model, we make an estimation of the time it would take for the observed clouds to reach equilibrium. Looking at clouds regions undergoing sublimation we estimate that the time it takes for the observed cloud particles to sublimate is shorter (2.1 hours) than it would take to reform similar ice particles in regions of cloud growth (3.2 hours). This discrepancy in sublimation and reformation time offers a possible explanation for why the equilibrium model overestimates the amount of ice. Furthermore, it indicates that atmospheric variability on these timescales has a tendency to reduce ice mass in PMCs.

This paper was conceived during a week's visit to Stockholm in September 2014, and the study has largely been led and executed by myself. Susanne Benze has been vital in reprocessing and analysing the OSIRIS data, and the thermodynamic equilibrium model used is a re-implementation of a model provided by Mark Hervig. The paper is written up by myself (with input from Susanne Benze), but the remaining co-authors have provided continuous feedback on the scientific analysis and linguistic formulation during the development of the paper.

REFERENCES

- Andrews, D. G.: An introduction to atmospheric physics, Cambridge University Press, New York, 2000.
- Backhouse, T. W.: The luminous cirrus cloud of June and July, *Meteorol. Mag*, 20, 133–133, 1885.
- Baldwin, M. P. and Dunkerton, T. J.: Stratospheric Harbingers of Anomalous Weather Regimes, *Science*, 294, 581–584, doi:10.1126/science.1063315, 2001.
- Baumgarten, G., Fiedler, J., and Rapp, M.: On microphysical processes of noctilucent clouds (NLC): observations and modeling of mean and width of the particle size-distribution, *Atmos. Chem. Phys.*, 10, 6661–6668, doi:10.5194/acp-10-6661-2010, 2010.
- Beig, G.: Long-term trends in the temperature of the mesosphere/lower thermosphere region: 1. Anthropogenic influences, *J. Geophys. Res.*, 116, doi:10.1029/2011JA016646, 2011.
- Beig, G., Keckhut, P., Lowe, R. P., Roble, R. G., Mlynczak, M. G., Scheer, J., Fomichev, V. I., Offermann, D., French, W. J. R., Shepherd, M. G., Semenov, A. I., Remsberg, E. E., She, C. Y., Lübken, F. J., Bremer, J., Clemesha, B. R., Stegman, J., Sigernes, F., and Fadnavis, S.: Review of mesospheric temperature trends, *R. Geophys.*, 41, doi:10.1029/2002RG000121, 1015, 2003.
- Bernath, P., McElroy, C., Abrams, M., Boone, C., Butler, M., Camy-Peyret, C., Carleer, M., Clerbaux, C., Coheur, P., Colin, R., et al.: Atmospheric chemistry experiment (ACE): mission overview, *Geophys. Res. Lett.*, 32, L15S01, 2005.
- Brasseur, G. and Solomon, S.: *Aeronomy of the middle atmosphere: Chemistry and physics of the stratosphere and mesosphere*, vol. 32, Springer, Dordrecht, 2005.
- Butler, C. J.: Possible observations of noctilucent clouds by Thomas Romney Robinson, *Weather*, 61, 143–144, doi:10.1256/wea.129.05, 2006.
- Carlotti, M., Dinelli, B. M., Raspollini, P., and Ridolfi, M.: Geo-fit approach to the analysis of limb-scanning satellite measurements, *Appl. Opt.*, 40, 1872–1885, doi:10.1364/AO.40.001872, 2001.

- Charron, M., Polavarapu, S., Buehner, M., Vaillancourt, P. A., Charette, C., Roch, M., Morneau, J., Garand, L., Aparicio, J. M., MacPherson, S., Pellerin, S., St-James, J., and Heilliette, S.: The Stratospheric Extension of the Canadian Global Deterministic Medium-Range Weather Forecasting System and Its Impact on Tropospheric Forecasts, *Mon. Weather. Rev.*, 140, 1924–1944, URL <http://search.proquest.com/docview/1022268916?accountid=10041>, 2012.
- Clancy, R. T. and Muhleman, D. O.: Ground-based microwave spectroscopy of the earth’s stratosphere and mesosphere, in: *Atmospheric remote sensing by microwave radiometry*, edited by Janssen, M. A., pp. 335–381, Wiley-InterScience, New York, 1993.
- Cook, J., Nuccitelli, D., Green, S. A., Richardson, M., Winkler, B., Painting, R., Way, R., Jacobs, P., and Skuce, A.: Quantifying the consensus on anthropogenic global warming in the scientific literature, *Environ. Res. Lett.*, 8, 024024, URL <http://stacks.iop.org/1748-9326/8/i=2/a=024024>, 2013.
- Darrin, A. and O’Leary, B. L.: *Handbook of space engineering, archaeology, and heritage*, CRC Press, Boca Raton, USA, 2009.
- Dee, D. P., Uppala, S. M., Simmons, A. J., Berrisford, P., Poli, P., Kobayashi, S., Andrae, U., Balmaseda, M. A., Balsamo, G., Bauer, P. and Bechtold, P., Beljaars, A. C. M., van de Berg, L., Bidlot, J., Bormann, N., Delsol, C., Dragani, R., Fuentes, M., Geer, A. J., Haimberger, L., Healy, S. B., Hersbach, H., Hólm, E. V., Isaksen, I., Kållberg, P., Köhler, M., Matricardi, M., McNally, A. P., Monge-Sanz, B. M., Morcrette, J.-J., Park, B.-K., Peubey, C., de Rosnay, P., Tavolato, C., Thépaut, J.-N., and Vitart, F.: The ERA-Interim reanalysis: configuration and performance of the data assimilation system, *Environ. Res. Lett.*, 137, 553–597, doi:10.1002/qj.828, 2011.
- Degenstein, D. A., Llewellyn, E. J., and Lloyd, N. D.: Volume emission rate tomography from a satellite platform, *Appl. Opt.*, 42, 1441–1450, doi:10.1364/AO.42.001441, 2003.
- DeLand, M. T. and Thomas, G. E.: Updated PMC trends derived from SBUV data, *J. Geophys. Res.*, 120, 2140–2166, doi:10.1002/2014JD022253, 2014JD022253, 2015.
- DeLand, M. T., Shettle, E. P., Thomas, G. E., and Olivero, J. J.: Latitude-dependent long-term variations in polar mesospheric clouds from SBUV version 3 PMC data, *J. Geophys. Res.*, 112, doi:10.1029/2006JD007857, d10315, 2007.
- Dupuy, E., Urban, J., Ricaud, P., Le Flochmoën, É., Lauté, N., Murtagh, D., De La Noë, J., El Amraoui, L., Eriksson, P., Forkman, P., et al.: Strato-mesospheric measurements of carbon monoxide with the Odin Sub-Millimetre Radiometer: Retrieval and first results, *Geophys. Res. Lett.*, 31, 101, 2004.

- Elgered, G.: Tropospheric radio-path delay from ground-based microwave radiometry, in: *Atmospheric remote sensing by microwave radiometry*, edited by Janssen, M. A., pp. 335–381, Wiley-InterScience, New York, 1993.
- Eriksson, P., Bühler, S., Davis, C., Emde, C., and Lemke, O.: ARTS, the atmospheric radiative transfer simulator, version 2, *J. Quant. Spectrosc. Radiat. Transfer*, 112, 1551–1558, doi:10.1016/j.jqsrt.2011.03.001, 2011.
- Farman, J. C., Gardiner, B. G., and Shanklin, J. D.: Large losses of total ozone in Antarctica reveal seasonal ClO_x/NO_x interaction, *Nature*, 315, 207–210, 1985.
- Feofilov, A. G. and Petelina, S. V.: Relation between mesospheric ice clouds, temperature, and water vapor determined from Odin/OSIRIS and TIMED/SABER data, *J. Geophys. Res.*, 115, doi:10.1029/2009JD013619, 2010.
- Fiedler, J., Baumgarten, G., and Von Cossart, G.: Mean diurnal variations of noctilucent clouds during 7 years of lidar observations at ALOMAR, in: *Ann. Geophysicae*, vol. 23, pp. 1175–1181, 2005.
- Fischer, H., Birk, M., Blom, C., Carli, B., Carlotti, M., von Clarmann, T., Delbouille, L., Dudhia, A., Ehhalt, D., Endemann, M., Flaud, J. M., Gessner, R., Kleinert, A., Koopman, R., Langen, J., López-Puertas, M., Mosner, P., Nett, H., Oelhaf, H., Perron, G., Remedios, J., Ridolfi, M., Stiller, G., and Zander, R.: MIPAS: an instrument for atmospheric and climate research, *Atmos. Chem. Phys.*, 8, 2151–2188, doi:10.5194/acp-8-2151-2008, 2008.
- Forkman, P., Eriksson, P., and Winnberg, A.: The 22 GHz radio-aeronomy receiver at Onsala Space Observatory, *J. Quant. Spectrosc. Radiat. Transfer*, 77, 23–42, doi:10.1016/S0022-4073(02)00073-0, 2003a.
- Forkman, P., Eriksson, P., Winnberg, A., Garcia, R., and Kinnison, D.: Longest continuous ground-based measurements of mesospheric CO, *Geophys. Res. Lett.*, 30, 1532, 2003b.
- Frisk, U., Hagström, M., Ala-Laurinaho, J., Andersson, S., Berges, J. C., Chabaud, J. P., Dahlgren, M., Emrich, A., Florén, H. G., Florin, G., Fredrixon, M., Gaier, T., Haas, R., Hirvonen, T., Hjalmarsson, A., Jakobsson, B., Jukkala, P., Kildal, P. S., Kollberg, E., Lassing, J., Lecacheux, A., Lehikoinen, P., Lehto, A., Mallat, J., Marty, C., Michet, D., Narbonne, J., Nexon, M., Olberg, M., Olofsson, A. O. H., Olofsson, G., Origné, A., Petersson, M., Piironen, P., Pons, R., Pouliquen, D., Ristorcelli, I., Rosolen, C., Rouaix, G., Räisänen, A. V., Serra, G., Sjöberg, F., Stenmark, L., Torchinsky, S., Tuovinen, J., Ullberg, C., Vinterhav, E., Wadefalk, N., Zirath, H., Zimmermann, P., and Zimmermann, R.: The Odin satellite, *Astron. Astrophys.*, 402, L27–L34, doi:10.1051/0004-6361:20030335, 2003.
- Gadsden, M.: Noctilucent clouds, *Space Science Reviews*, 33, 279–334, doi:10.1007/BF00196999, 1982.

- Grundmann, R.: Transnational environmental policy: Reconstructing ozone, Routledge, London, 2001.
- Gumbel, J. and Karlsson, B.: Intra- and inter-hemispheric coupling effects on the polar summer mesosphere, *Geophys. Res. Lett.*, 38, n/a–n/a, doi:10.1029/2011GL047968, 114804, 2011.
- Hervig, M. E. and Stevens, M. H.: Interpreting the 35 year SBUV PMC record with SOFIE observations, *J. Geophys. Res.*, 119, 12,689–12,705, doi:10.1002/2014JD021923, 2014JD021923, 2014.
- Holton, J. R.: An Introduction to Dynamic Meteorology, vol. 48 of *International Geophysics Series*, Academic Press, 3 edn., San Diego, 1992.
- Hultgren, K. and Gumbel, J.: Tomographic and spectral views on the lifecycle of polar mesospheric clouds from Odin/OSIRIS, *J. Geophys. Res.*, 119, 14,129–14,143, doi:10.1002/2014JD022435, 2014JD022435, 2014.
- Hultgren, K., Gumbel, J., Degenstein, D., Bourassa, A., Lloyd, N., and Stegman, J.: First simultaneous retrievals of horizontal and vertical structures of Polar Mesospheric Clouds from Odin/OSIRIS tomography, *J. Atmos. Sol.-Terr. Phys.*, 104, 213 – 223, doi:http://dx.doi.org/10.1016/j.jastp.2013.06.013, 2013.
- Hunten, D. M., Turco, R. P., and Toon, O. B.: Smoke and dust particles of meteoric origin in the mesosphere and stratosphere, *J. Atmos. Sci.*, 37, 1342–1357, 1980.
- Jesse, O.: Auffallende Abenderscheinungen am Himmel, *Meteorol. Z.*, 2, 311–312, 1885.
- Jones, A., Urban, J., Murtagh, D. P., Eriksson, P., Brohede, S., Haley, C., Degenstein, D., Bourassa, A., von Savigny, C., Sonkaew, T., Rozanov, A., Bovensmann, H., and Burrows, J.: Evolution of stratospheric ozone and water vapour time series studied with satellite measurements, *Atmos. Chem. Phys.*, 9, 6055–6075, 2009.
- Jones, S. and Gillan, A.: The day the snow came - and Britain stopped, *The Guardian*, URL <http://www.theguardian.com/uk/2009/feb/02/snow-brings-britain-travel-chaos>, 2009.
- Karlsson, B., Körnich, H., and Gumbel, J.: Evidence for interhemispheric stratosphere-mesosphere coupling derived from noctilucent cloud properties, *Geophys. Res. Lett.*, 34, doi:10.1029/2007GL030282, 2007.
- Keating, G. M., Tolson, R. H., and Bradford, M. S.: Evidence of long term global decline in the Earth's thermospheric densities apparently related to anthropogenic effects, *Geophys. Res. Lett.*, 27, 1523–1526, URL <http://dx.doi.org/10.1029/2000GL003771>, 2000.

- Kim, B.-M., Son, S.-W., Min, S.-K., Jeong, J.-H., Kim, S.-J., Zhang, X., Shim, T., and Yoon, J.-H.: Weakening of the stratospheric polar vortex by Arctic sea-ice loss, *Nature communications*, 5, 2014.
- Kirkwood, S., Dalin, P., and Réchou, A.: Noctilucent clouds observed from the UK and Denmark - trends and variations over 43 years, *Ann. Geophysicae*, 26, 1243–1254, doi:10.5194/angeo-26-1243-2008, 2008.
- Kley, D. and Russell III, J.: SPARC Assessment of Upper Tropospheric and Stratospheric Water Vapour, *SPARC newsletter*, 16, 11–18, 2001.
- Leslie, R. J.: Sky Glows, *Nature*, 32, 245, doi:10.1038/032245a0, 1885.
- Lindzen, R. S.: Turbulence and stress owing to gravity wave and tidal breakdown, *J. Geophys. Res.*, 86, 9707–9714, 1981.
- Livesey, N., Van Snyder, W., Read, W., and Wagner, P.: Retrieval algorithms for the EOS Microwave limb sounder (MLS), *IEEE Trans. Geosci. Remote Sensing*, 44, 1144–1155, doi:10.1109/TGRS.2006.872327, 2006.
- Llewellyn, E. J., Lloyd, N. D., Degenstein, D. A., Gattinger, R. L., Petelina, S. V., Bourassa, A. E., Wiensz, J. T., Ivanov, E. V., McDade, I. C., Solheim, B. H., McConnell, J. C., Haley, C. S., von Savigny, C., Sioris, C. E., McLinden, C. A., Griffioen, E., Kaminski, J., Evans, W. F., Puckrin, E., Strong, K., Wehrle, V., Hum, R. H., Kendall, D. J., Matsushita, J., Murtagh, D. P., Brohede, S., Stegman, J., Witt, G., Barnes, G., Payne, W. F., Piché, L., Smith, K., Warshaw, G., Deslauniers, D. L., Marchand, P., Richardson, E. H., King, R. A., Wevers, I., McCreath, W., Kyrölä, E., Oikarinen, L., Leppelmeier, G. W., Auvinen, H., Mégie, G., Hauchecorne, A., Lefèvre, F., de La Nöe, J., Ricaud, P., Frisk, U., Sjöberg, F., von Schéele, F., and Nordh, L.: The OSIRIS instrument on the Odin spacecraft, *Can. J. Phys.*, 82, 411–422, doi:10.1139/p04-005, 2004.
- Lloyd, N. D. and Llewellyn, E. J.: Deconvolution of blurred images using photon counting statistics and maximum probability, *Canadian Journal of Physics*, 67, 89–94, doi:10.1139/p89-013, 1989.
- Lopez-Puertas, M. and Taylor, F. W.: *Non-LTE Radiative Transfer in the Atmosphere*, Series on Atmospheric, Oceanic and Planetary Physics, World Scientific Co. Pte. Ltd., River Edge, 2001.
- Lossow, S., Urban, J., Schmidt, H., Marsh, D. R., Gumbel, J., Eriksson, P., and Murtagh, D.: Wintertime water vapor in the polar upper mesosphere and lower thermosphere: first satellite observations by Odin submillimeter radiometer, *J. Geophys. Res.*, 114, D10 304, 2009.
- Louet, J. and Bruzzi, S.: ENVISAT mission and system, in: *Geoscience and Remote Sensing Symposium, 1999. IGARSS'99 Proceedings. IEEE 1999 International*, vol. 3, pp. 1680–1682, IEEE, 1999.

- Manney, G. L., Harwood, R. S., MacKenzie, I. A., Minschwaner, K., Allen, D. R., Santee, M. L., Walker, K. A., Hegglin, M. I., Lambert, A., Pumphrey, H. C., Bernath, P. F., Boone, C. D., Schwartz, M. J., Livesey, N. J., Daffer, W. H., and Fuller, R. A.: Satellite observations and modeling of transport in the upper troposphere through the lower mesosphere during the 2006 major stratospheric sudden warming, *Atmos. Chem. Phys.*, 9, 4775–4795, doi:10.5194/acp-9-4775-2009, 2009.
- Marsh, D., Smith, A., Brasseur, G., Kaufmann, M., and Grossmann, K.: The existence of a tertiary ozone maximum in the high-latitude middle mesosphere, *Geophys. Res. Lett.*, 28, 4531–4534, doi:10.1029/2001GL013791, URL <http://dx.doi.org/10.1029/2001GL013791>, 2001.
- McInturff, R. M.: Stratospheric warmings: Synoptic, dynamic and general-circulation aspects, Tech. Rep NASA-RP-1017, Washington, DC, 1978.
- McNoleg, O.: The integration of GIS, remote sensing, expert systems and adaptive co-kriging for environmental habitat modeling of the Highland Haggis using object-oriented, fuzzy-logic and neural-network techniques, *Comput. Geosci.*, 22, 585 – 588, doi:http://dx.doi.org/10.1016/0098-3004(95)00131-X, 1996.
- Megnér, L.: Minimal impact of condensation nuclei characteristics on observable Mesospheric ice properties, *J. Atmos. Sol.-Terr. Phys.*, 73, 2184 – 2191, doi:http://dx.doi.org/10.1016/j.jastp.2010.08.006, layered Phenomena in the Mesopause Region, 2011.
- Mills, M. J., Toon, O. B., and Thomas, G. E.: Mesospheric sulfate aerosol layer, *J. Geophys. Res.*, 110, n/a–n/a, doi:10.1029/2005JD006242, URL <http://dx.doi.org/10.1029/2005JD006242>, d24208, 2005.
- Molina, M. J. and Rowland, F. S.: Stratospheric sink for chlorofluoromethanes: chlorine atom-catalysed destruction of ozone, *Nature*, 249, 810–812, 1974.
- Morgan, D. and Beech, E.: UPDATE 4-Blizzard paralyzes U.S. mid-Atlantic; two killed, Reuters, <http://www.reuters.com/article/2010/02/06/weather-usa-idUSN0614831920100206>, retrieved on: 2015-07-21, 2010.
- Murphy, D. M. and Koop, T.: Review of the vapour pressures of ice and supercooled water for atmospheric applications, *Q. J. R. Meteorol. Soc.*, 131, 1539–1565, 2005.
- Murtagh, D., Frisk, U., Merino, F., Ridal, M., Jonsson, A., Stegman, J., Witt, G., Eriksson, P., Jiménez, C., Megie, G., Noë, J. d. L., Ricaud, P., Baron, P., Pardo, J. R., Hauchcorne, A., Llewellyn, E. J., Degenstein, D. A., Gattinger, R. L., Lloyd, N. D., Evans, W. F. J., McDade, I. C., Haley, C., Sioris, C., von Savigny, C., Solheim, B. H., McConnell, J. C., Strong, K., Richardson, E. H., Leppelmeier, G. W., Kyrölä, E., Auvinen, H., and Oikarinen, L.: An overview of the Odin atmospheric mission, *Can. J. Phys.*, 80, 309–319, 2002.

- NASA's Earth Observatory: Stratosphere Influences Winter Weather, <http://earthobservatory.nasa.gov/IOTD/view.php?id=36972>, retrieved on: 2015-07-19, 2009.
- Ning, T., Haas, R., Elgered, G., and Willén, U.: Multi-technique comparisons of 10Å years of wet delay estimates on the west coast of Sweden, *Journal of Geodesy*, 86, 565–575, doi:10.1007/s00190-011-0527-2, 2012.
- Nordh, H. L., Von Schéele, F., Frisk, U., Ahola, K., Booth, R. S., Encrenaz, P. J., Hjalmarson, Å., Kendall, D., Kyrölä, E., Kwok, S., Lecacheux, A., Leppelmeier, G., Llewellyn, E. J., Mattila, K., Mégie, G., Murtagh, D., Rougeron, M., and Witt, G.: The Odin orbital observatory, *Astronomy & Astrophysics*, 402, L21–L25, 2003.
- Offermann, D., Hoffmann, P., Knieling, P., Koppmann, R., Oberheide, J., and Steinbrecht, W.: Long-term trends and solar cycle variations of mesospheric temperature and dynamics, *J. Geophys. Res.*, 115, doi:10.1029/2009JD013363, d18127, 2010.
- Pawson, S., Steinbrecht, W., Charlton-Perez, A., Fujiwara, M., Karpechko, A., Petropavlovskikh, I., Urban, J., and Weber, M.: Update on Global Ozone: Past, Present, and Future, in: *Scientific Assessment of Ozone Depletion: 2014, Global Ozone Research and Monitoring Project – Report No. 55*, chap. 2, World Meteorological Organization, Geneva, Switzerland, 2014.
- Pérot, K., Urban, J., and Murtagh, D. P.: Unusually strong nitric oxide descent in the Arctic middle atmosphere in early 2013 as observed by Odin/SMR, *Atmos. Chem. Phys.*, 14, 8009–8015, doi:10.5194/acp-14-8009-2014, 2014.
- Pierrehumbert, R. T.: *Principles of planetary climate*, Cambridge University Press, New York, 2010.
- Plane, J.: The role of sodium bicarbonate in the nucleation of noctilucent clouds, *Ann. Geophysicae*, 18, 807–814, doi:10.1007/s00585-000-0807-2, 2000.
- Pueschel, R. F., Verma, S., Rohatschek, H., Ferry, G. V., Boiadjieva, N., Howard, S. D., and Strawa, A. W.: Vertical transport of anthropogenic soot aerosol into the middle atmosphere, *J. Geophys. Res.*, 105, 3727–3736, doi:10.1029/1999JD900505, 2000.
- Pumphrey, H. C., Filipiak, M., Livesey, N., Schwartz, M., Boone, C., Walker, K., Bernath, P., Ricaud, P., Barret, B., Clerboux, C., Jarnot, R., Manney, G., and Waters, J.: Validation of middle-atmosphere carbon monoxide retrievals from MLS on Aura, *J. Geophys. Res.*, 112, D24S38, 2007.
- Rapp, M. and Lübken, F.-J.: Polar mesosphere summer echoes (PMSE): Review of observations and current understanding, *Atmospheric Chemistry and Physics*, 4, 2601–2633, doi:10.5194/acp-4-2601-2004, 2004.

- Rapp, M. and Thomas, G. E.: Modeling the microphysics of mesospheric ice particles: Assessment of current capabilities and basic sensitivities, *J. Atmos. Sol.-Terr. Phys.*, 68, 715–744, 2006.
- Rees, D., Barnett, J., and Labitzke, K.: COSPAR International Reference Atmosphere: 1986. Pt. 2: Middle atmosphere models, *Adv. Space. Res.*, 10, 1990.
- Rees, W. G.: *Physical Principles of Remote Sensing*, Cambridge University Press, Cambridge, United Kingdom, 2001.
- Roble, R. and Dickinson, R.: How will changes in carbon dioxide and methane modify the mean structure of the mesosphere and thermosphere?, *Geophys. Res. Lett.*, 16, 1441–1444, 1989.
- Rodgers, C.: *Inverse methods for atmospheric sounding: Theory and practice*, World Scientific, Singapore, 2000.
- Rohlfs, K. and Wilson, T. L.: *Tools of Radio Astronomy*, Springer-Verlag, Berlin, 2008.
- Ronan, P.: File:EM_spectrum.svg - Wikimedia Commons, https://commons.wikimedia.org/wiki/File:EM_spectrum.svg, retrieved on: 2015-07-19, 2007.
- Scheiben, D., Straub, C., Hocke, K., Forkman, P., and Kämpfer, N.: Observations of middle atmospheric H₂O and O₃ during the 2010 major sudden stratospheric warming by a network of microwave radiometers, *Atmos. Chem. Phys.*, 12, 7753–7765, doi:10.5194/acp-12-7753-2012, 2012.
- Schoeberl, M., Douglass, A., Hilsenrath, E., Bhartia, P., Beer, R., Waters, J., Gunson, M., Froidevaux, L., Gille, J., Barnett, J., et al.: Overview of the EOS Aura mission, *IEEE Trans. Geosci. Remote Sensing*, 44, 1066–1074, 2006.
- Schröder, W.: Were noctilucent clouds caused by the Krakatoa eruption? A case study of the research problems before 1885, *Bulletin of the American Meteorological Society*, 80, 2081–2085, 1999.
- Shepp, L. A. and Vardi, Y.: Maximum likelihood reconstruction for emission tomography, *IEEE Transactions on Medical Imaging*, 1, 113–122, 1982.
- Shettle, E. P., DeLand, M. T., Thomas, G. E., and Olivero, J. J.: Long term variations in the frequency of polar mesospheric clouds in the Northern Hemisphere from SBUV, *Geophys. Res. Lett.*, 36, doi:10.1029/2008GL036048, 102803, 2009.
- Solomon, S. C., Hays, P., and Abreu, V. J.: Tomographic inversion of satellite photometry, *Appl. Opt.*, 23, 3409–3414, 1984.

- Steck, T., Höpfner, M., von Clarmann, T., , and Grabowski, U.: Tomographic retrieval of atmospheric parameters from infrared limb emission observations, *Appl. Opt.*, 44, doi:10.1364/AO.44.003291, 2005.
- Stevens, M. H., Gumbel, J., Englert, C. R., Grossmann, K. U., Rapp, M., and Hartogh, P.: Polar mesospheric clouds formed from space shuttle exhaust, *Geophys. Res. Lett.*, 30, 2003.
- Stolarski, R. S. and Cicerone, R. J.: Stratospheric chlorine: a possible sink for ozone, *Can. J. Chem.*, 52, 1610–1615, 1974.
- Straub, C., Murk, A., and Kämpfer, N.: MIAWARA-C, a new ground based water vapor radiometer for measurement campaigns, *Atmos. Meas. Tech.*, 3, 1271–1285, doi:10.5194/amt-3-1271-2010, 2010.
- Svensmark, H. and Friis-Christensen, E.: Variation of cosmic ray flux and global cloud coverage—a missing link in solar-climate relationships, *J. Atmos. Sol.-Terr. Phys.*, 59, 1225 – 1232, doi:http://dx.doi.org/10.1016/S1364-6826(97)00001-1, 1997.
- Thomas, G.: Is the polar mesosphere the miner’s canary of global change?, *Advances in Space Research*, 18, 149–158, 1996.
- Thomas, G. E., McPeters, R. D., and Jensen, E. J.: Satellite observations of polar mesospheric clouds by the solar backscattered ultraviolet spectral radiometer: Evidence of a solar cycle dependence, *J. Geophys. Res.*, 96, 927–939, doi:10.1029/90JD02312, 1991.
- Thomas, G. E., Olivero, J. J., Deland, M., and Shettle, E. P. E. P.: Comment on “Are noctilucent clouds truly a “Miner’s Canary” for Global Change?”, *Eos, Transactions American Geophysical Union*, 84, 352–353, 2003.
- Thomas, R. J. and Donahue, T. M.: Analysis of Ogo 6 observations of the O I 5577-A tropical nightglow, *Journal of Geophysical Research*, 77, 3557–3565, doi:10.1029/JA077i019p03557, 1972.
- Thompson, D., Seidel, D., Randel, W., Zou, C., Butler, A., Mears, C., Osso, A., Long, C., and Lin, R.: The mystery of recent stratospheric temperature trends, *Nature*, 491, 692–697, 2012.
- Urban, J., Lautié, N., Murtagh, D. P., Eriksson, P., Kasai, Y., Lossow, S., Dupuy, E., Noë, J. D. L., Frisk, U., Olberg, M., Flochmoën, E. L., and Ricaud, P.: Global observations of middle atmospheric water vapour by the Odin satellite: an overview, *PPS*, 55, 1093–1102, 2007.
- von Clarmann, T., De Clercq, C., Ridolfi, M., Höpfner, M., and Lambert, J.-C.: The horizontal resolution of MIPAS, *Atmos. Meas. Tech.*, 2, 47–54, doi:10.5194/amt-2-47-2009, 2009.

- von Savigny, C., Petelina, S. V., Karlsson, B., Llewellyn, E. J., Degenstein, D. A., Lloyd, N. D., and Burrows, J. P.: Vertical variation of NLC particle sizes retrieved from Odin/OSIRIS limb scattering observations, *Geophys. Res. Lett.*, 32, n/a–n/a, doi:10.1029/2004GL021982, 107806, 2005.
- von Savigny, C., Sinnhuber, M., Bovensmann, H., Burrows, J. P., Kallenrode, M.-B., and Schwartz, M.: On the disappearance of noctilucent clouds during the January 2005 solar proton events, *Geophys. Res. Lett.*, 34, n/a–n/a, doi:10.1029/2006GL028106, 102805, 2007.
- von Zahn, U.: Are noctilucent clouds a “Miner’s Canary” for global change?, *Eos, Transactions American Geophysical Union*, 84, 261–264, doi:10.1029/2003EO280001, 2003.
- Witt, G.: The nature of noctilucent clouds., in: *Space Research IX*, vol. 1, pp. 157–169, 1969.
- WMO: Assessment for Decision-Makers: Scientific Assessment of Ozone Depletion: 2014, in: *Global Ozone Research and Monitoring Project - Report No. 56*, World Meteorological Organization, Geneva, Switzerland, 2014.

ACKNOWLEDGEMENTS

Though my name stands alone on the front of this thesis I would be remiss if I did not thank the persons making it possible for me to work on these projects and guide me through the paths and hurdles of scientific investigation. In particular, I owe a big thanks to my main supervisor Patrick Eriksson. His support, patience and always on-point critical questions have without a doubt help me feel confident in myself and my work. My co-supervisor Peter Forkman similarly deserves gratitude for 5 years of great cooperation, and for always making me feel at home at Råö. Finally, I am forever grateful to Donal Murtagh for warmly accepting me as a PhD-student in the research group and for always having an open door, both literally and metaphorically.

Besides these three persons, I owe a big thanks to all my colleagues and friends in Göteborg, including Jo who unfortunately left us all too soon. Whether its discussing the intricacies of statistics/atmospheric physics/backgammon/politics or love (pick your topic) you have made these past few years a blast. In particular thanks to everyone at West Coast Jitterbugs for accepting to dance with me, and everyone at the Chalmers Sailing Society for daring to sail with me!

Furthermore, I would never be where I am today without the support and love from my great family, thank you all!

My last and largest thanks is extended to the Swedish taxpayer, who in the end allowed me to spend 5 years in their country looking at clouds.

